

Weierstraß-Institut
für Angewandte Analysis und Stochastik
Leibniz-Institut im Forschungsverbund Berlin e. V.

Preprint

ISSN 2198-5855

hMRI – A toolbox for using quantitative MRI
in neuroscience and clinical research

Evelyne Balteau¹, Karsten Tabelow², John Ashburner³, Martina F. Callaghan³,
Bogdan Draganski^{4,5}, Gunther Helms⁶, Ferath Kherif⁴, Tobias Leutritz⁷,
Antoine Lutti⁴, Christophe Phillips¹, Enrico Reimer⁷, Lars Ruthotto⁸, Maryam Seif⁹,
Nikolaus Weiskopf⁷, Gabriel Ziegler¹⁰, Siawoosh Mohammadi¹¹

submitted: July 31, 2018 (revision: September 7, 2018)

¹ GIGA Institute, University of Liège, Liège, Belgium

² Weierstrass Institute, Mohrenstr. 39, 10117 Berlin, Germany, E-Mail: karsten.tabelow@wias-berlin.de

³ Wellcome Trust Centre for Neuroimaging, London, UK

⁴ Laboratory for Research in Neuroimaging, Department of Clinical Neuroscience,
Lausanne University Hospital and University of Lausanne, Switzerland

⁵ Department of Neurology, Max Planck Institute for Human Cognitive and Brain Sciences, Leipzig, Germany

⁶ Department of Medical Radiation Physics, Lund University, Lund, Sweden

⁷ Department of Neurophysics, Max Planck Institute for Human Cognitive and Brain Sciences, Leipzig, Germany

⁸ Emory University, Atlanta, USA

⁹ University of Zurich, Switzerland

¹⁰ Otto von Guericke Universität Magdeburg, Germany

¹¹ Medical Center Hamburg-Eppendorf, Hamburg, Germany

No. 2527
Berlin 2018



Key words and phrases. Quantitative MRI, in-vivo histology, microstructure, Multi-Parameter Mapping, relaxometry, SPM toolbox.

Edited by
Weierstraß-Institut für Angewandte Analysis und Stochastik (WIAS)
Leibniz-Institut im Forschungsverbund Berlin e. V.
Mohrenstraße 39
10117 Berlin
Germany

Fax: +49 30 20372-303
E-Mail: preprint@wias-berlin.de
World Wide Web: <http://www.wias-berlin.de/>

hMRI – A toolbox for using quantitative MRI in neuroscience and clinical research

Evelyne Balteau, Karsten Tabelow, John Ashburner, Martina F. Callaghan,
Bogdan Draganski, Gunther Helms, Ferath Kherif, Tobias Leutritz,
Antoine Lutti, Christophe Phillips, Enrico Reimer, Lars Ruthotto, Maryam Seif,
Nikolaus Weiskopf, Gabriel Ziegler, Siawoosh Mohammadi

ABSTRACT. Neuroscience and clinical researchers are increasingly interested in quantitative magnetic resonance imaging (qMRI) due to its sensitivity to micro-structural properties of brain tissue such as axon, myelin, iron and water concentration. We introduce the hMRI-toolbox, an easy-to-use tool openly available on GitHub, for qMRI data handling and processing, presented together with a tutorial and example dataset. This toolbox allows the estimation of high-quality multi-parameter qMRI maps (longitudinal and effective transverse relaxation rates R_1 and R_2^* , proton density PD and magnetisation transfer MT saturation) that can be used for accurate delineation of subcortical brain structures and calculation of standard and novel MRI biomarkers of tissue microstructure. Embedded in the Statistical Parametric Mapping (SPM) framework, it can be readily combined with existing SPM toolboxes for estimating diffusion MRI parameter maps, and it benefits from the extensive range of established SPM tools for high-accuracy spatial registration and statistical inferences. The hMRI-toolbox is an efficient, robust and simple framework for investigating qMRI data in neuroscience and clinical research.

1. INTRODUCTION

Quantitative MRI (qMRI) finds increasing interest in neuroscience and clinical research due to its greater specificity and its sensitivity to micro-structural properties of brain tissue such as axon, myelin, iron and water concentration (Tofts 2004; Assaf and Basser 2005; Draganski et al. 2011; Lorio et al. 2014; Lorio et al. 2016a; Stüber et al. 2014). This interest arises from the fact that qMRI, unlike conventional weighted MRI, aims to estimate absolute physical metrics, free from instrumental biases (Lutti et al. 2010; Weiskopf et al. 2013). The quantitative nature of the data is especially useful as it allows comparison across sites, time points and participants, enabling longitudinal studies and multi-centre trials (Deoni et al. 2008; Weiskopf et al. 2013). Combining qMRI with biophysical modelling enables the *in vivo* characterisation of key microscopic brain tissue parameters which previously could only be achieved with *ex vivo* histology. This concept is called *in vivo* histology using MRI (hMRI, Weiskopf et al. 2015).

The estimation of quantitative and semi-quantitative metrics commonly includes the effective transverse relaxation rate ($R_2^* = 1/T_2^*$), the longitudinal relaxation rate ($R_1 = 1/T_1$), the proton density (PD), the magnetisation transfer (MT) saturation and a number of diffusion MRI (dMRI) metrics (Draganski et al. 2011). However, the majority of fundamental and clinical neuroscience studies either refrain from acquiring qMRI data or the quantitative approach is limited to dMRI only, because for this technique standardised qMRI imaging protocols (such as the protocol for the Human Connectome Project (Sotiropoulos et al. 2013)) and processing software (see a summary in Soares et al. 2013) are readily available. These studies are therefore at best sensitive to axonal properties but less so to complementary microstructural tissue features such as myelin, water or iron content that can be revealed using bias free estimates of R_2^* , R_1 , PD and MT saturation.

The neuroscience and clinical research community lacks a standardised qMRI implementation to estimate these parameters and handle a wide diversity of data types. For example, R_2^* is often estimated using gradient recalled echo data acquired with multiple echo times (TE) to create high resolution maps that show strong contrast between different types of brain tissue (Bernstein, King, and Zhou 2004). Similarly, PD and R_1 can be derived from two acquisitions varying the excitation flip angle (Wang, Riederer, and Lee 1987; Deoni, Peters, and Rutt 2005; Deoni 2007; Schabel and Morrell

2008; Helms et al. 2011; Liberman, Louzoun, and Ben Bashat 2013; Heule, Ganter, and Bieri 2015; Baudrexel et al. 2016). For accurate estimation of the qMRI parameters, an implementation must adequately correct for instrumental biases such as inhomogeneous transmit (Lutti et al. 2010) and receive fields (Volz et al. 2012; Mezer et al. 2016). Such correction should be based on the additional mapping of these fields, but the implementation should also provide solutions when bias fields have not been measured. For example in clinical settings, MR sequences for estimating instrumental biases are often unavailable due to time, hardware or software constraints. For such studies, the facility to correct for instrumental biases retrospectively using image processing methods that do not rely on additional MRI acquisitions is highly desirable.

For spatial processing and group level statistical analysis, the established tools that can handle qMRI data without losing the quantitative nature of the underlying qMRI techniques are primarily designed for diffusion MRI (see for example TBSS in FSL (Smith et al. 2006) and TRACULA (Yendiki et al. 2011) in FreeSurfer), while a number of custom made tools have been developed based on established neuroimaging software. For example, see applications of the FreeSurfer surface projection software (Dale and Sereno 1993; Fischl et al. 1999; Fischl and Dale 2000) to compare quantitative relaxation and susceptibility data on the cortex (Marques, Khabipova, and Gruetter 2017), or usage of the VBM framework (Ashburner and Friston 2000) to process qMRI data across the whole brain at a voxel-by-voxel level (Büchel et al. 2004 and Mohammadi et al. 2012 for dMRI metrics, and Table 1 for R_2^* , R_1 , PD and MT saturation). The majority of the studies in Table 1 took advantage of voxel-based quantification (VBQ), a novel approach introduced by Draganski et al. 2011 and developed to preserve the quantitative nature of the maps generated by the comprehensive multi-parameter mapping (MPM) approach (Helms et al. 2008; Helms et al. 2009; Weiskopf et al. 2011; Weiskopf et al. 2013).

Developed at 3T, the MPM approach spans data acquisition, modelling and bias correction of three multi-echo spoiled gradient echo volumes to generate R_2^* , R_1 , PD , as well as semi-quantitative MT saturation maps. This framework enables time-efficient whole brain mapping with high isotropic resolution of 800 μm in 24 min (Callaghan et al. 2015b) or 1 mm isotropic resolution in 18 min at 3T (Papp et al. 2016) and has even enabled the acquisition of ultra-high-resolution quantitative maps at 400 μm at 7T (Trappel et al. 2017). This framework has been used in a variety of fundamental and clinical neuroscience studies (Table 1) focussing on: (a) improving the segmentation of deep grey matter structures, (b) evaluating the myelin and iron concentration in the brain and spinal cord, (c) linking structure and function in the cortex, and (d) using the MPM parameter maps as proxies for biophysical tissue models.

In this paper, we present the hMRI-toolbox, a comprehensive open-source toolbox that streamlines all the processing steps required to generate R_2^* , R_1 , PD and MT saturation maps and provides appropriate spatial processing for group analyses. The flexible nature of the toolbox makes it applicable to a wide range of data types, from the full MPM protocol to subsets of it, including e.g. single contrast echo trains for mapping R_2^* or variable flip angle data for mapping of R_1 and PD using multi-echo or even single-echo data. The toolbox is embedded in the SPM framework (<http://www.fil.ion.ucl.ac.uk/spm/software/spm12/>), profiting from the highly accurate spatial registration into a common space and the variety of established statistical inference schemes. The spatial processing part of the toolbox can be applied to any set of rotationally-invariant qMRI maps, including a number of diffusion MRI parameters and all common qMRI metrics.

Reference	Predominant tissue feature My Fe Vol	qMRI parameters	Subjects	Remarks
Studies demonstrating improved volumetry				
Helms et al. 2009	– ✓	MT	49 C	Improved segmentation of deep brain grey matter structures using magnetization transfer (MT) parameter maps.
Lambert et al. 2013 Studies of myelin and/or iron	– ✓	R_1, R_2^*, MT, PD^*	34 C	Brainstem segmentation using a modified multivariate mixture of Gaussians based on MPMs.
Draganski et al. 2011	✓ ✓	R_1, R_2^*, MT	26 C	A fingerprint of age-dependent brain atrophy and underlying microstructural changes in myelin, iron deposits and water.
Lambert et al. 2013	✓ ✓	R_1, R_2^*, MT, PD^*	26 C	Characterizing aging in the human brainstem using quantitative multimodal MRI analysis.
Freund et al. 2013	✓ – ✓	R_1, MT	13 P / 18 C	Atrophic and microstructural changes of corticospinal axons and sensorimotor cortical areas observed in the first months after spinal cord injury.
Callaghan et al. 2014	✓ ✓	R_1, R_2^*, MT, PD^*	138 C	A whole-brain pattern of age-associated microstructural differences in the asymptomatic population providing insight into the neurobiology of aging.
Lorio et al. 2014	✓ ✓	R_1, R_2^*, MT, PD^*	96 C	Deviation of volume changes assessed with VBM using standard T1-weighted or MT maps, attributed to age-related iron changes.
Lorio et al. 2016b	✓ ✓	R_1, R_2^*, MT, PD^*	120 C	Impact of microstructural properties of brain tissue-myelination, iron, and water content on automated measures of brain morphology using VBM.
Steiger, Weiskopf, and Bunzeck 2016	✓ ✓ –	R_2^*, MT	31 C	Age-related increase of iron correlated negatively with iron and myelin in the ventral striatum, which predicted individual memory performance.
Carey et al. 2017b	✓ ✓ –	R_2^*, MT, R_1, PD^*	93 C	Delineation of cortical myelin profiles across cortical depths and mapping of tissue water sensitive parameters (PD^*).
Ziegler et al. 2018	✓ ✓	R_2^*, MT	15 P / 18 C	Trauma-induced neuroplastic processes in brain and spinal cord including neurodegenerative processes associated with iron and myelin changes.
Studies linking structure and function in the cortex				
Dick et al. 2012	✓ – –	R_1 (& fMRI)	9 C	Combining structural R_1 mapping with functional tonotopy to reveal their interrelation within the primary auditory areas (A1 and R).
Sereno et al. 2013	✓ – –	R_1 (& fMRI)	6 C	Combined structural R_1 mapping and functional retinotopy revealed boundaries visible in the R_1 maps that correspond to recognised retinotopic borders.
Lutti et al. 2014	✓ – –	R_1 (& fMRI)	–	Review about using high-resolution mapping of R_1 as an index of cortical myelination.
Helbing et al. 2015	✓ – –	R_1 (& M/EEG)	5 C	Combining electrophysiology with MPMs demonstrating microstructure-function relationship.
Whitaker et al. 2016	✓ – ✓	R_1, MT	297 C	Assessment of layer-specific microstructure in adolescence development and comparison to volume differences.
Carey et al. 2017a	✓ – –	R_1 (& fMRI)	10 C	Functional and R_1 mapping demonstrate overlap between articulator and R1 myelin proxy maps in pre and post-central regions.
Dick et al. 2017	✓ – –	R_1 (& fMRI)	8 C	Functional and R_1 mapping demonstrate strong concordance in the degree of cortical myelination and the strength of tonotopic activation across several auditory cortical regions.
Studies combining MPMs and biophysical models				
Callaghan et al. 2015a	✓ ✓ –	R_2^*, MT, R_1, PD^*	138 C	Combining MPM and a general linear relaxometry model to describe the biophysical relation of R_1 on iron, myelin, and water content.

Mohammadi et al. 2015	-	✓	-	MT (& dMRI)	38 C	Using MPM-based MT and diffusion-MRI-based tract fibre density as proxies for estimating myelin and axon densities as well as the g-ratio.
Weiskopf et al. 2015	✓	✓	✓	R_2^* , MT , R_1 , PD^*	-	Review about in vivo histology using MRI.
Callaghan, Mohammadi, and Weiskopf 2016	✓	✓	✓	R_2^* , MT , R_1 , PD^*	12 C / 30 C	Using a biophysical relation between R_{11} , MT , and R_2^* to generate synthetic quantitative maps.
Ellerbrock and Mohammadi 2018	✓	✓	-	MT , PD (& dMRI)	22 C	Comparing different proxies for myelin and fibre volume fractions using MPMs and diffusion MRI.

Table 1: Studies using predecessors of the $hMRI$ -toolbox and the MPM acquisition to make inference on myelin (My), iron (Fe), or the volume (Vol) measured by voxel-based morphometry (VBM). Note that all studies used Siemens MRI scanners. Abbreviations: R_1 =longitudinal relaxation rate, R_2^* = effective transverse relaxation rate, PD^* = (effective) proton density, MT = magnetisation transfer, C = controls, P = patients, dMRI= diffusion MRI, fMRI= functional MRI, MEG= magnetoencephalography, EEG= electroencephalography.

2. BACKGROUND

2.1. The MPM protocol. The MPM multi-echo protocol was introduced in Weiskopf and Helms 2008 and Weiskopf et al. 2013 for estimating the longitudinal relaxation rate R_1 , the effective transverse relaxation rate R_2^* , the proton density PD and the magnetisation transfer MT and generalises a number of acquisition protocols. It typically involves acquiring six to eight images at different echo times (TE) for each of the PD-, T1- and MT-weighted acquisitions in an RF and gradient spoiled gradient echo sequence (referred to as T1w, PDw and MTw echoes, respectively). The hMRI-toolbox can flexibly deal with a large range of site- and study-specific acquisition schemes, from the full MPM protocol to subsets of it, including single contrast echo trains for mapping R_2^* or variable flip angle data for mapping of R_1 and PD using multi-echo or single-echo data. Example MPM acquisition protocols can be found at <http://hmri.info>.

2.2. Overview theory of MPM signal model. We give here, and in Fig. 1, a short overview of the theory underlying the qMRI map creation process. For a detailed outline of the theory and the estimation procedures applied in the hMRI-toolbox see A.

The signal from the multi-echo PDw, T1w and MTw acquisitions can be described by the Ernst equation (Ernst and Anderson 1966; Helms, Dathe, and Dechent 2008; Helms et al. 2008). The effective transverse relaxation rate R_2^* can then be derived from the TE dependence of the signal. The unified description of the multi-echo data from all three contrasts into a single model, denoted as ESTATICS (Weiskopf et al. 2014), provides a more robust estimation of R_2^* with a higher signal-to-noise ratio compared to separate estimations (Fig. 1a). Using approximations of the signal equations for small repetition time TR and small flip angles α , the longitudinal relaxation rate R_1 , the A^* map (proportional to the proton density PD) and the magnetisation transfer MT can be estimated. At this point (Fig. 1b), the generated maps are biased by B_1 transmit f_T (Fig. 1c) and receive f_R (Fig. 1d) field inhomogeneities. The hMRI-toolbox provides correction methods for these bias fields based on specific B_1 transmit and receive field measurements or image processing methods. While f_T influences the local flip angle and hence all three (R_1 , PD , MT) maps are affected, the RF sensitivity bias field f_R only influences the PD map (in the absence of subject motion).

The toolbox can also handle the situation where only a subset of data is available. For example, R_2^* , R_1 and PD can still be estimated when no MTw acquisitions are acquired, R_2^* alone can be estimated when neither MTw nor T1w acquisitions are available (single multi-echo PDw data). R_1 , PD and MT maps can be generated from single echo PDw, T1w and MTw images, not requiring multi-echo acquisitions. We note that the theory and map creation tools also encompass the creation of R_1 maps from other variable flip angle approaches, such as DESPOT1 (Deoni, Peters, and Rutt 2005) or creating R_2^* maps from multi-echo data, such as certain susceptibility mapping/weighted imaging approaches.

3. METHODS

3.1. Toolbox documentation and installation.

3.1.1. Download. The latest version of the toolbox can be downloaded from the hMRI-toolbox page (<http://hmri.info>) as a zip file (containing the last official release) or by cloning the git repository (<https://github.molgen.mpg.de/hMRI-group/Toolbox>) to keep up-to-date with the latest incremental developments.

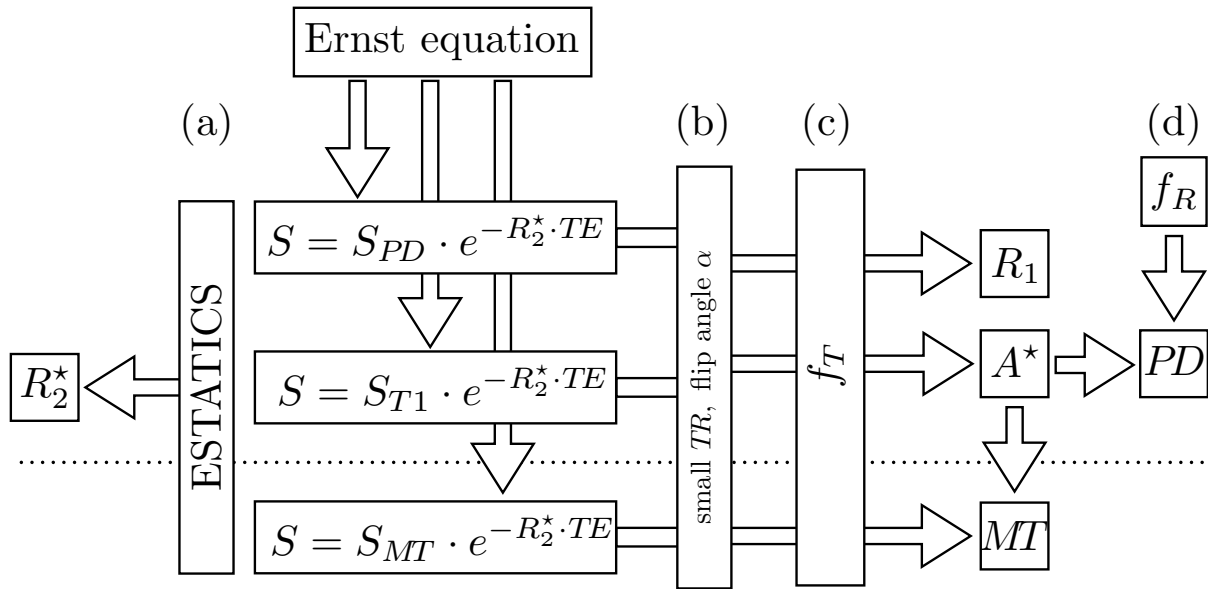


FIGURE 1. Overview of qMRI map generation from the weighted imaging and reference MPM data. The signal S is modelled by the Ernst equation with an exponential decay depending on the echo time TE . The longitudinal relaxation rate R_1 , the effective transverse relaxation rate R_2^* , the proton density PD and the magnetisation transfer MT are estimated from the data, using approximations for small repetition time TR and small flip angles α . The transmit and receive bias fields f_T and f_R are used to correct for instrumental biases.

3.1.2. *Documentation.* Updated documentation is available as a Wiki (<https://github.molgen.mpg.de/hMRI-group/Toolbox/wiki>) on the git repository, and includes installation instructions, an example dataset, a tutorial and a detailed description of the implemented functionalities.

3.1.3. *Software requirements.* The toolbox has been developed and tested with MATLAB versions 8.0 (R2012b) to 9.3 (R2017b) and SPM12 versions r6906 (12.3) and r7219 (12.4). Since the hMRI developments will be synchronised with SPM developments, it is recommended to use the most recent SPM release (<http://www.fil.ion.ucl.ac.uk/spm/software/spm12/>) to benefit from the latest developments.

3.1.4. *Installation.* It is suggested that users clone the git repository of the hMRI-toolbox locally and keep the version up-to-date, each time they start a new study. However, we would advise against updating the toolbox during a study (i.e. analysing a subset of data with different versions of the toolbox). The installation procedure allows users to manage the hMRI-toolbox repository independently from their SPM installation, thanks to a *redirection* script. This is especially convenient when a version control system is used for SPM as well. Installation instructions are provided in the online Wiki and summarised below for convenience:

- clone the repository into a `<path-to-your-hMRI>` directory independent from the SPM installation,
- create a directory `<path-to-your-spm>/toolbox/hMRI` in your SPM installation directory,
- copy `tbx_cfg_hmri_redirect.m` from `<path-to-your-hMRI>/install/` into the newly created `<path-to-your-spm>/toolbox/hMRI` directory,
- add the SPM installation and the hMRI_Toolbox directories to the MATLAB path,

- start MATLAB and launch SPM.

The hMRI toolbox is then available as an SPM toolbox from the SPM Batch GUI (Batch button in the SPM Menu), under `SPM > Tools > hMRI Tools` (Fig. 2).

3.1.5. License. The hMRI-toolbox is free but copyright software, distributed under the terms of the GNU General Public License as published by the Free Software Foundation (as given in file `Copyright.txt`). Further details on “copyleft” can be found at <http://www.gnu.org/copyleft/>.

In particular, the hMRI-toolbox is supplied as is. No formal support or maintenance is provided or implied. Since the toolbox was developed for academic research, it comes with no warranty and is not intended for clinical use.

3.2. MPM example dataset. An MPM example dataset from a healthy subject for demonstrating the hMRI-toolbox features was acquired on a 3T Prisma system (Siemens Healthcare, Erlangen, Germany) at the Wellcome Trust Centre for Neuroimaging, London, UK. This dataset can be downloaded from <https://hmri.info>. The study was approved by the local ethics committee and informed written consent was obtained from the participant prior to scanning. Data were anonymised and de-faced.

Rapid calibration data were acquired at the outset of the MRI session to map and consequently correct for inhomogeneities in the B_1 transmit field (Lutti et al. 2010; Lutti et al. 2012). Eleven spin-echo and stimulated-echo pairs were acquired with the nominal flip angles varying from 115° to 65° in 5° decrements.

These were followed by acquisition of 3D multi-echo RF and gradient spoiled gradient echo acquisitions with predominantly PD, T1 or MT weighting similar to the MPM protocol described in Callaghan et al. 2015b. The flip angle was 6° for the PDw- and MTw-volumes and 21° for the T1w acquisition. MT-weighting was achieved through the application of a Gaussian RF pulse 2 kHz off-resonance with 4ms duration and a nominal flip angle of 220° . The RF spoiling phase increment was 137° and the spoiler moment was 6π across a voxel. The data were acquired with whole-brain coverage at an isotropic resolution of $800\mu\text{m}$ using a field of view (FoV) of 256mm head-foot, 224mm anterior-posterior (AP), and 179mm right-left (RL). Gradient echoes were acquired with alternating readout gradient polarity at eight equidistant echo times ranging from 2.30 to 18.40ms in steps of 2.30ms using a readout bandwidth of 488Hz/pixel. Only six echoes were acquired for the MTw acquisition in order to maintain a TR of 25ms for all gradient echo volumes. To accelerate the data acquisition, partially parallel imaging using the GRAPPA algorithm (Griswold et al. 2002) was employed in each phase-encoded direction (AP and RL) with forty reference lines and a speed up factor of two. The acquisition time for each set of spoiled multi-echo gradient echo volumes was 7.08min. The data were acquired using the body coil for signal transmission and a 64 channel head and neck array for signal reception. Each dataset was acquired with a 30° rotation of the sagittal plane so that any eye-related motion artefact propagated to the neck/inferior cerebellum rather than the cortex.

Prior to the acquisition of each spoiled gradient echo series, two additional 3D rapid, unaccelerated, low resolution (8 mm isotropic, same FoV) volumes were acquired with the same spoiled gradient echo sequence, one with the 64-channel head and neck array coil and the other with the body coil. A single echo, with a TE of 2.20 ms, was acquired in each case using a 6° flip angle and a TR of 6.00 ms. The acquisition time for each of these calibration volumes was 5.90 s.

These data were used to correct for the position-specific sensitivity modulation of the array coil by approximately removing the receive field sensitivity bias (Papp et al. 2016). To test the performance of this correction, the participant performed a yaw rotation (i.e. about the z-axis) within the confines of the 64 channel coil prior to the acquisition of the MTw dataset before returning to his original position

Acquisitions	
1	B_1 mapping protocol
2	RF sensitivity measurements
3	PDw-echoes acquisition
<i>Large yaw rotation (i.e. about the z-axis) within the confines of the 64-channel coil</i>	
4	RF sensitivity measurements
5	MTw-echoes acquisition
<i>Back to initial position</i>	
6	RF sensitivity measurements
7	T1w-echoes acquisition

TABLE 2. The temporal succession of the acquisitions in the MPM example dataset.

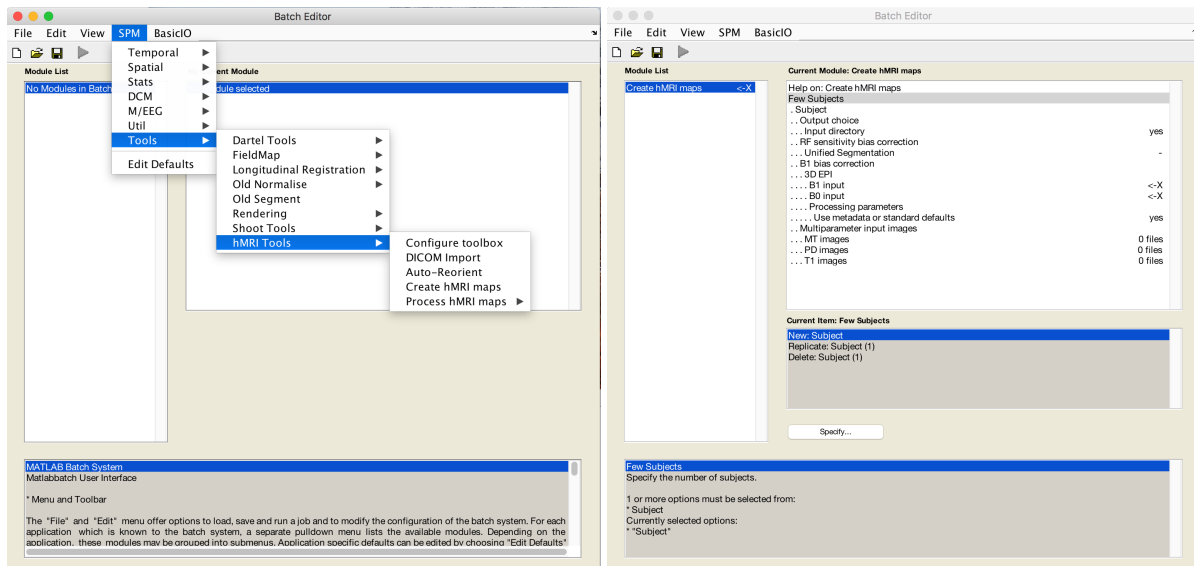


FIGURE 2. Left: After installation (Section 3.1), the hMRI toolbox can be started from the SPM menu of the batch editor. Five options include toolbox configuration, DICOM import, re-orientation of the data to MNI space, creation and processing of the hMRI maps. Right: Input mask for the map creation part of the toolbox.

centred within the head coil for the T1w acquisition. A summary of this protocol is given in Table 2 highlighting the temporal succession of the events. This protocol and other example MPM protocols can be found at <https://hmri.info>.

3.3. Organisation of the toolbox. The hMRI-toolbox is organised into five main modules (Fig. 2): *Configure toolbox*, *DICOM import*, *Auto-reorient*, *Create hMRI maps* and *Process hMRI maps*. While the *Configure Toolbox* and *Process hMRI maps* modules can be run for a group of subjects, the *DICOM Import*, *Auto-reorient* and *Create hMRI maps* modules must be run for each subject and each session separately (if several datasets acquired per subject, e.g. in a longitudinal study). A brief description of each module is provided below and details can be found in the Appendices.

3.4. Configure toolbox module. The hMRI-toolbox provides the user with a set of default acquisition and processing parameters for most common acquisition protocols without any further customisation. However, customisation is possible and necessary to broaden the toolbox usability to a wider range of protocols. Therefore, the *Configure toolbox* module allows the user to select either standard or customised default parameters, to match the user's own site- or protocol-specific setup and to be used in the subsequent modules (see details in C.1).

3.5. DICOM import module. *DICOM import* is a tool to convert DICOM data into NIfTI files. During conversion, the whole DICOM header is stored as JSON-encoded metadata in a file along side the NIfTI images. This feature is now implemented in SPM12 r7219 (November 2017) following the hMRI-toolbox implementation. The hMRI-toolbox also provides metadata handling functionalities to retrieve parameter values and store processing parameters in the JSON-encoded metadata file (see Table 4 for an example of processing information stored as metadata). Detailed description of the DICOM import module, the metadata handling tools and BIDS compliance aspects (Gorgolewski et al. 2016) is provided in B.

3.6. Auto-reorient module. The reorientation of the images towards a standard pose, setting the anterior commissure at the origin and both anterior and posterior commissure (AC/PC) in the same axial plane, as defined in MNI space (Mazziotta et al. 1995; Mazziotta et al. 2001a; Mazziotta et al. 2001b), is a common step that increases the consistency in individual head positions prior to normalisation or segmentation. For example, SPM's segmentation (Ashburner and Friston 2005) is sensitive to the initial orientation of the images. Therefore, *Auto-reorient* provides a simple tool for automatically and uniformly reorienting a set of images prior to any further processing including multi-parameter map calculation. Note, that the reorientation modifies the orientation information in each image header, but the reoriented images are not resliced. For more details, see C.2.

3.7. Create hMRI maps module. The *Create hMRI maps* module computes quantitative as well as semi-quantitative estimates of R_2^* , R_1 , PD and MT saturation from unprocessed multi-echo T1w, PDw and MTw spoiled gradient echo acquisitions. The map creation module corrects the qMRI estimates for spatial receive (Section 3.7.3) and transmit (Section 3.7.2) field inhomogeneities.

3.7.1. Multi-parameter input images. The module takes the (possibly reoriented) series of multi-echo spoiled gradient echo images as input for the creation of quantitative as well as semi-quantitative maps (Fig. 3) of R_2^* , R_1 , PD and MT (Helms, Dathe, and Dechent 2008; Helms et al. 2008; Weiskopf et al. 2013; Weiskopf et al. 2014) as described in the Background Section 2 and A. The number and quality of the output maps depends on the contrasts (PDw, T1w, MTw) and number of echoes available, and on the availability of additional bias field measurements. A single multi-echo PDw contrast allows for the calculation of a single R_2^* map. If T1w images are additionally provided, R_1 and PD maps will also be generated. The MT map estimation requires the acquisition of additional MTw images. The map creation also involves optional correction for B_1^+ (B_1 transmit) bias field f_T (Section 3.7.2) and the B_1^- (RF receive sensitivity) bias field f_R (Section 3.7.3) as well as spoiling imperfections (Yarnykh 2010; Preibisch and Deichmann 2009).

3.7.2. B_1 (transmit) bias correction. The map creation module includes the determination of B_1 transmit bias field maps (f_T expressed in p.u. of the nominal flip angle) for transmit bias correction of the quantitative data. Several methods are implemented. Depending on the choice of the specific method the GUI requires the user to provide adequate input files. Further details on the supported correction methods can be found in C.3 and the respective original publications (Lutti et al. 2010; Lutti et al. 2012; Weiskopf et al. 2013; Weiskopf et al. 2011; Yarnykh 2007; Chung et al. 2010).

3.7.3. Receiver RF sensitivity bias correction. Three options are available to correct for RF receive sensitivity bias (f_R) within the *Create hMRI maps* module. Two of them rely on measured RF sensitivity maps (`Single` or `Per contrast` options) while the third method is data driven (`Unified Segmentation` option: no input sensitivity map required). Although not recommended, it is possible to disable RF sensitivity correction altogether by selecting the `None` option. While options `Single` and `Unified Segmentation` assume that the sensitivity profile is consistent between

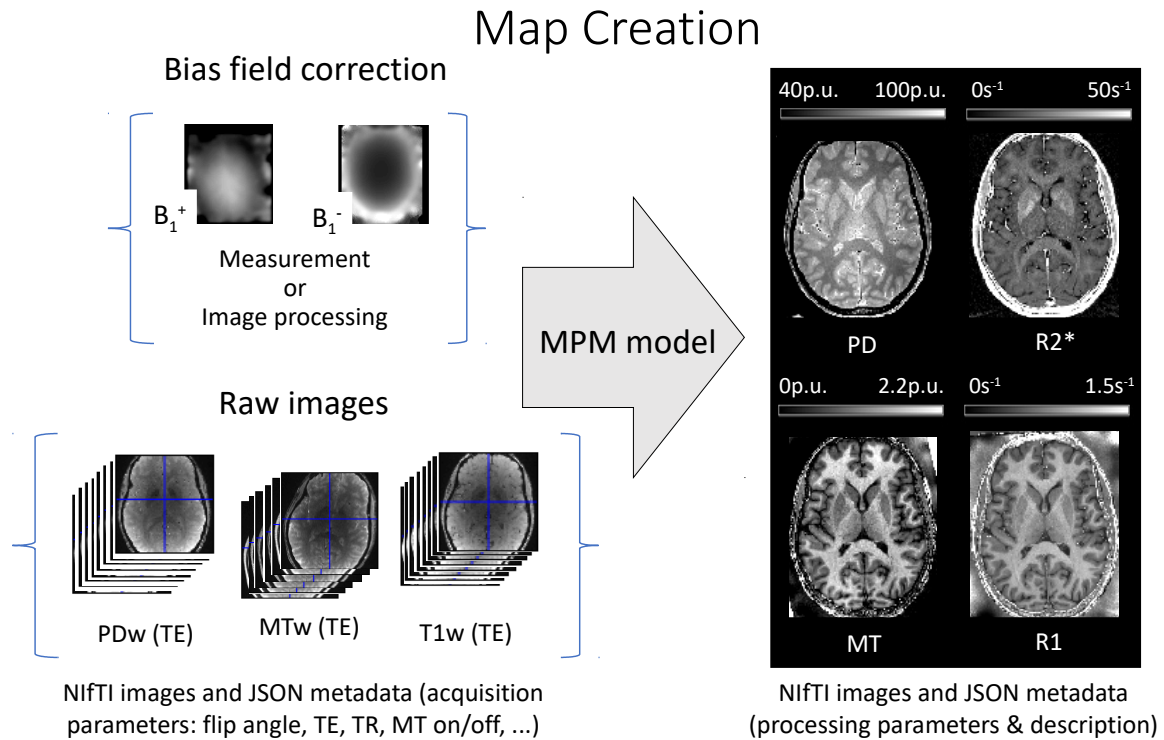


FIGURE 3. Map creation workflow illustrated for the MPM example dataset (Section 3.2 and Table 2). The MPM protocol includes three multi-echo spoiled gradient echo scans with predominant T1-, PD- and MT-weighting achieved by an appropriate choice of the repetition time, the flip angle and the off-resonance MT pulse. Optional RF transmit (B_1^+) and receive (B_1^-) field measurements can be added to the protocol, improving the quality of instrumental bias correction in the MPM maps. Alternatively, these reference measurements can be, to a limited extent, replaced by dedicated image processing steps that are provided by the toolbox. The map creation module generates PD , R_1 , MT and R_2^* maps. For each map, a JSON metadata file is created, which contains information about the processing pipeline of each image (see example in Table 4).

contrasts (i.e. small inter-contrast subject movement is assumed), the `Per contrast` option accounts for inter-contrast variation in RF sensitivity profile due to larger subject motion (Papp et al. 2016). Details on the different RF sensitivity bias correction methods can be found in C.4 and in the respective publications (Papp et al. 2016; Weiskopf et al. 2013).

3.7.4. Output. By default, the estimated quantitative maps are output into a `Results` subdirectory within the folder of the first PDw echo. Alternatively, a user-defined folder for the output of the toolbox can be selected in which the `Results` directory will be created. The estimated qMRI maps are saved in the `Results` directory, with supplementary files are output in the `Results/Supplementary` subfolder. The basename for all qMRI maps is derived from the first echo of the PDw image series, see Table 3 for brief description. If data is reprocessed, a new sub-folder is created.

3.8. Process hMRI maps module. The *Process hMRI maps* module provides dedicated tools and tissue probability maps for the spatial processing of quantitative MRI maps based on the corresponding SPM framework. The spatial processing pipeline for hMRI data relies on three main operational steps (Fig. 4): (1) segmentation (Ashburner and Friston 2005; Draganski et al. 2011; Lorio et al. 2016a), (2)

Results directory	Description
<firstPDfileName>_MT.[nii json]	Estimated MT saturation map in p.u.
<firstPDfileName>_PD.[nii json]	Estimated PD map in p.u.
<firstPDfileName>_R1.[nii json]	Estimated R_1 map in s^{-1}
<firstPDfileName>_R2s_OLS.[nii json]	Estimated R_2^* map in s^{-1} (ESTATICS)
Results/Supplementary directory	Description
hMRI_map_creation_rfparams_params.json	RF sensitivity bias correction parameters (measured sensitivity maps)
hMRI_map_creation_b1map_params.json	B_1 transmit map estimation: acquisition and processing parameters
hMRI_map_creation_job_create_maps.json	Create hMRI maps: acquisition and processing parameters
hMRI_map_creation_mpm_params.json	Acquisition and processing parameters used for the current job
hMRI_map_creation_quality_assessment.json	Quality assessment results (Appendix D)
<firstSESTEfileName>_B1map.[nii json]	Estimated B_1 bias field f_T map (p.u.)
<firstSESTEfileName>_B1ref.[nii json]	Anatomical reference for B_1 bias field correction
<firstPDfileName>_MTw_OLSfit_TEzero.[nii json]	MTw echoes extrapolated to $TE = 0$
<firstPDfileName>_PDw_OLSfit_TEzero.[nii json]	PDw echoes extrapolated to $TE = 0$
<firstPDfileName>_R2s.[nii json]	Estimated R_2^* map from simple exponential fit (PDw echoes)
<firstPDfileName>_T1w_OLSfit_TEzero.[nii json]	T1w echoes extrapolated to $TE = 0$

TABLE 3. Output files from the *Create hMRI maps* module using the SE/STE B_1 mapping and per-contrast RF sensitivity bias correction.

non-linear spatial registration into common space (Ashburner 2007) and (3) tissue-weighted smoothing (Draganski et al. 2011), using three different sub-modules that are further detailed in the Appendix, Table 3. Furthermore, a fully integrated processing pipeline is provided as an additional sub-module to facilitate standard data processing without the need to combine the individual steps in this module. Details on the three sub-modules and the integrated pipeline are provided in C.5.

3.9. Statistical analysis. The standard SPM statistical analysis and modelling approaches such as mass-univariate General Linear Modelling can be applied to the spatially processed maps, see, e.g., Draganski et al. 2011 and Freund et al. 2013. Additionally, the multiple parameter maps lend themselves to multi-variate analyses approaches as well (Draganski et al. 2011).

4. DISCUSSION AND OUTLOOK

This paper introduced the hMRI-toolbox, which is embedded in the SPM framework and allows for the estimation and processing of four quantitative MRI maps: the longitudinal and effective transverse relaxation rates R_1 and R_2^* , the proton density PD and the (semi-quantitative) magnetisation transfer saturation MT . This includes a comprehensive summary of the MPM signal model as well as the currently available correction methods for the various bias sources that, if not corrected for, might impair the quantification. Finally, the processing steps for a dedicated VBM-style of image analysis (denoted as the VBQ approach), which preserve the quantitative nature of the maps, were presented.

The name of the toolbox (h-MRI) originates from the idea of *in vivo histology* of tissue microstructure using MRI (Weiskopf et al. 2015). Hereby, the quantitative parameter maps generated with this toolbox provide key input parameters for biophysical models that are designed to non-invasively estimate specific microstructure tissue properties, see Table 1 for example studies.

Considerations and interpretation of the MPM approach. While the signal model (see A for details) used in this toolbox is based on the Ernst equation and thus provides a comprehensive means of calculating a collection of physical quantitative (and semi-quantitative) parameters, including PD , R_2^* , R_1 and MT , we would like to emphasise that more sophisticated signal models can be derived to relate the parameters more directly to the underlying biophysical mechanisms and tissue characteristics.

The contrast provided by the R_2^* metric is associated with different realisation of iron deposits (for a review, see e.g. Edwards et al. 2018), myelination of axons (Marques, Khabipova, and Gruetter 2017), their orientation (Oh et al. 2013) and chemical exchange (Does 2018). Multi-compartment models can

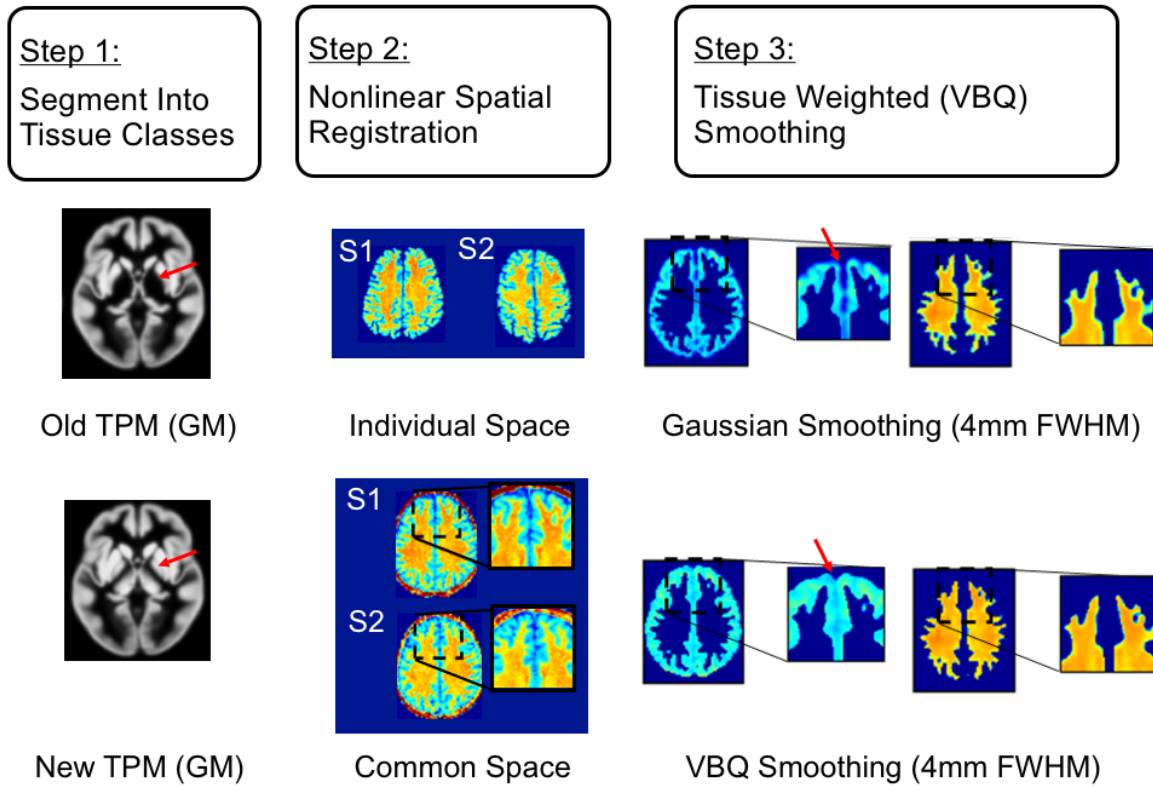


FIGURE 4. Overview of the spatial processing module. It consists of three steps: (1) segmentation, (2) highly parametrised non-linear spatial registration, and (3) tissue-weighted smoothing. The segmentation step (1) uses novel tissue-probability maps (TPMs), designed to take advantage of the better contrast of the MPMs for improved segmentation (exemplified for the deep-grey matter by the arrow in (1)). The non-linear spatial registration step into common space (2) reduces inter-individual anatomical differences (exemplified for R_1 maps of subject one and two, S1 and S2, respectively). To further reduce residual anatomical differences (see magnification boxes in (2)) and enhance statistical inference, the qMRI maps can be spatially smoothed (3) using the voxel-based quantification (VBQ) smoothing procedure. As compared to Gaussian smoothing, VBQ smoothing avoids bias in the qMRI maps (e.g. see arrows in (3), highlighting a rapid decline in R_1 values at tissue boundaries only after Gaussian smoothing. The VBQ smoothing is detailed in Eq. (18) and Draganski et al. 2011). The sub-figure (1) has been adapted from (Lorio et al. 2016a), sub-figures (2) and (3) from Mohammadi and Callaghan 2018.

be used, e.g., to separately describe the orientation-dependence of myelinated fibre pathways in R_2^* parameter maps (e.g., Lee et al. 2016; Alonso-Ortiz, Levesque, and Pike 2017; Wharton and Bowtell 2012).

At a given field strength, the R_1 contrast is determined by the micro-structural tissue properties such as the local mobility of water molecules, the macromolecular content and the local concentration of paramagnetic ions such as iron or gadolinium-based contrast agents. It has been shown that R_1 depends linearly on these tissue properties (Fatouros and Marmarou 1999; Fatouros et al. 1991; Kaneoke et al. 1987; Shuter et al. 1998; Donahue et al. 1994; Kamman et al. 1988; Fullerton, Potter,

and Dornbluth 1982; Gelman et al. 2001). The R_2^* and MT metrics can be used to describe the dependence of R_1 on these components (Callaghan et al. 2015a).

MT saturation is a semi-quantitative proxy measure of the bound-pool water fraction (Helms et al. 2008). As such, it provides information about the macromolecular content of the micro-structural environment and is often used as a marker for myelin content, see, e.g., Freund et al. 2013 and Callaghan et al. 2014. The MT saturation map differs from the commonly used MT ratio (MTR; percent reduction in steady state signal) by explicitly removing the bias introduced by the spatially varying T_1 relaxation time and B_1 -transmit field (Helms et al. 2008). Additional minor corrections for B_1 transmit field inhomogeneity in the MT maps were applied as described in Weiskopf et al. 2013. The reduced spatially varying bias leads, e.g., to a higher contrast in deep brain structures than MTR and to reduced variance in the data (Callaghan, Mohammadi, and Weiskopf 2016). However, the MT saturation measure does not only depend on the bound-pool fraction but also on the exchange between the bound and free water pools (see e.g. Tofts, Steens, and van Buchem 2004). A more direct measure of the bound-pool fraction is provided by quantitative MT (qMT), which requires more time-consuming data acquisition, typically limiting the MT map spatial resolution (e.g., 2mm isotropic in Stikov et al. 2011).

Sources of bias in qMRI and limitations to bias corrections. Correction of instrumental characteristics and artefacts is an essential prerequisite for quantitative MRI. Sources of biases and artefacts include primarily transmit and receive fields, imperfect spoiling, T_2^* -bias and head motion. The artefact correction methods provided in the hMRI-toolbox are highly flexible, offering solutions to process reference measurements (e.g. transmit/receive field measurements carried out with a number of customised or product sequences) to correct for instrumental biases artefacts, as well as achieve optimal results even when no adequate measurements are available.

The ideal imaging protocol includes dedicated measurements of transmit and receive field inhomogeneities, which are typically based on customised sequences (Fig. 5a-d for RF receive bias correction, and Fig. 6a for B_1 transmit bias correction). When customised sequences are not available, a standard spoiled gradient echo product sequence can be used to acquire data for low-resolution receive field mapping. Similarly, when not available, customised reference and calibration sequences such as 3D_EPI (Lutti et al. 2010; Lutti et al. 2012) or 3D_AFI (Yarnykh 2007) for correction of B_1 transmit effects can be replaced by manufacturer's service sequences such as TFL_B1_map (Chung et al. 2010) or RF_map (as examples on Siemens scanners). The toolbox provides the option to process data from several different B_1 transmit bias field mapping techniques or to use B_1 transmit bias field maps pre-computed outside the toolbox (see section 3.7.2 and C.3).

The measured transmit and receive fields can be affected by diverse sources of error leading to imperfect corrections. For example, residual misalignment between measured receive (or transmit) field and the spoiled gradient echo images could be one reason for such imperfections. RF receive sensitivity maps can also suffer from residual modulations by the receive field of the body coil, which serves as a reference and whose inhomogeneity is not accounted for (C.4). Moreover, at 7T where body coils are not available, the currently implemented RF sensitivity measurements and bias correction approach are not applicable. Similarly, B_1 transmit field mapping techniques can be inaccurate. For a comparison of the frequently used B_1 -transmit field mapping techniques and a description of their respective accuracy and sources of uncertainty we refer to Lutti et al. 2010 and Pohmann and Scheffler 2013.

When no transmit and/or receive field inhomogeneity maps have been measured, which often happens in clinical settings due to time constraints, the toolbox provides the option to use image processing methods based on the Unified Segmentation approach (Ashburner and Friston 2005) for B_1 transmit bias correction (UNICORT, Weiskopf et al. 2011, see Fig. 6b) or RF sensitivity bias correction (Fig. 5e). The Unified Segmentation approach takes advantage of the fact that bias corrections can be applied post hoc in good approximation for small read-out flip angles and short TR (Helms, Dathe, and Dechent 2008). This requires no additional acquisition time but produces quantitative maps of

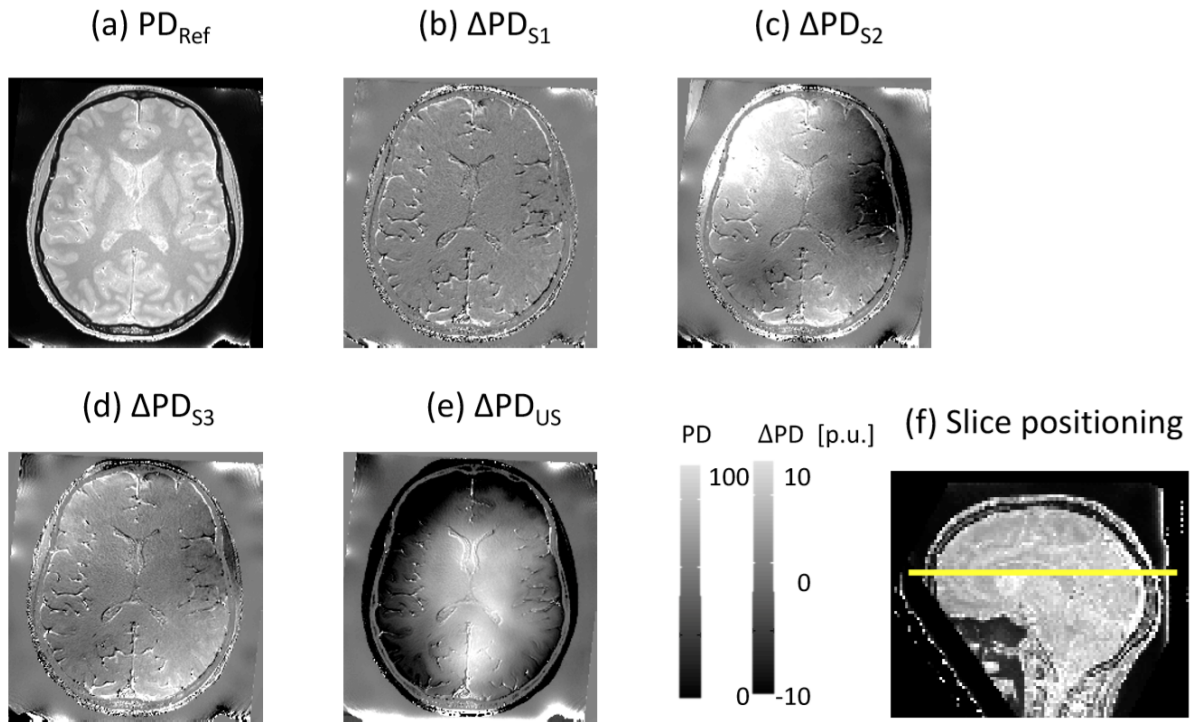


FIGURE 5. Comparison of different available RF sensitivity bias field correction methods (C.4) demonstrated on the MPM example dataset (Section 3.2) and PD difference maps. (a) PD map calculated using the reference correction method (PD_{Ref}), following the approach in Papp et al. 2016, requiring three sensitivity maps, each acquired directly before the respective PDw, MTw and T1w contrasts. (b-d) Difference between PD_{Ref} and PD maps calculated from PDw and T1w images corrected by a single sensitivity map, acquired directly before the PDw images (b: ΔPD_{S1}), the MTw images (c: ΔPD_{S2}) and the T1w images (d: ΔPD_{S3}), respectively. Due to the large overt movement preceding the acquisition of the MTw images and corresponding RF sensitivity measurement (see Table 2), there is a large discrepancy between head position for that specific RF sensitivity measurement on the one hand and head positions for the PDw and T1w images used to generate the PD map on the other hand. As a result, errors in (c) are much larger than in (b) and (d). (e) Difference between PD_{Ref} and the PD map corrected for RF sensitivity bias using the Unified Segmentation approach (ΔPD_{US}). The body coil sensitivity profile, not corrected for in the reference method, modulates the PD difference map in (e). (f) Sagittal view of PD map in (a) depicting the position of the slice shown in (a-e).

lesser accuracy with some residual receive and/or transmit field modulation (Weiskopf et al. 2011; Baudrexel et al. 2016) compared to a correction with measured references. Note that the Unified Segmentation approach, whether applied for B_1 transmit (UNICORT) or RF sensitivity bias correction, has been optimised for the Siemens TIM-TRIO MR system using the body RF coil for transmission and the 32-channel receive head coil. The corrections will perform appropriately for coils with similar transmit or receive field profiles, but might require further adjustments otherwise (see Weiskopf et al. 2011 for UNICORT optimisation). For more details, see (Callaghan et al. 2016) and the hMRI wiki (the latter also provides further information on customized usage).

The proposed MPM protocol uses RF and gradient spoiling to minimise unwanted transverse net magnetisation. Imperfect spoiling, which depends on the precise sequence protocol settings, can leave a residual bias in the R_1 map if no further correction is used (Preibisch and Deichmann 2009; Yarnykh

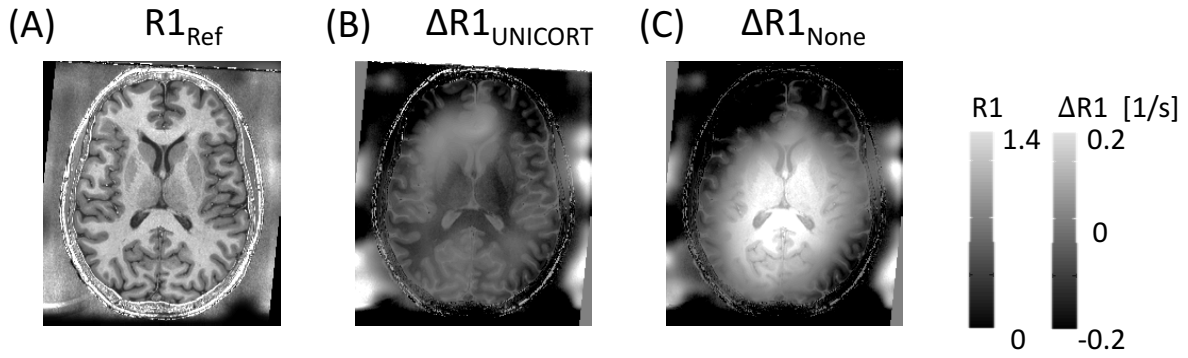


FIGURE 6. Comparison of two different available transmit field correction methods demonstrated on longitudinal relaxation rate (R_1) maps. (A) The $R_{1,Ref}$ map is depicted after using the reference correction method, following the B_1 mapping approach by Lutti et al. 2012. (B) The difference between the reference map $R_{1,Ref}$ and the R_1 map derived with UNICORT B_1 transmit bias correction (image processing method, no additional measurement required, see Weiskopf et al. 2011 for details). (C) The difference between the reference map $R_{1,Ref}$ and the R_1 map derived without B_1 transmit bias correction. (B) shows a residual modulation across the slice while (C) is strongly biased by the B_1 transmit inhomogeneity across the slice. The slice location in (A-C) is depicted in Fig.5f.

2010). For specific MPM protocols using the customised sequences, the hMRI-toolbox provides a correction for imperfect spoiling, see Eq. (15) in A.5. By default this correction is disabled but can be enabled through the toolbox customisation provided by the *Configure toolbox* module (C.1 and the hMRI-toolbox Wiki).

The estimation of PD maps can be biased by T_2^* relaxation effects if not accounted for (Eq. (4) in A). Two correction methods, based on extrapolation of the data to $TE = 0$ (Ellerbrock and Mohammadi 2018) or relying on the estimated R_2^* maps respectively, are implemented in the toolbox (Balteau et al. 2018). These correction methods require a number of echoes to be acquired for a robust fit of the exponential decay to derive $TE = 0$ magnitude images and R_2^* maps. In the case of a single-echo variable flip angle dataset, the T_2^* -weighting correction cannot be applied and the estimated PD and (to a much lesser extent) the R_1 and MT maps will be biased by T_2^* -modulations. Note that the JSON metadata file associated with the respective PD parameter map contains information about the processing steps and thus of potential T_2^* modulation.

Head motion is widely recognised as a major source of artefacts in MR images, with severe consequences on quantitative MRI and morphological measures of the brain (Callaghan et al. 2015b; Weiskopf et al. 2014; Reuter et al. 2015). While the extraction of quantitative measures of image quality is currently under investigation, visual inspection remains largely considered as the gold-standard in the field (Rosen et al. 2018). The hMRI-toolbox provides summary measures of the head motion during each spoiled gradient echo acquisition (intra-scan motion) as well as measures of the inter-scan head displacements (Castella et al. 2018 and D). These intra- and inter-scan head motion measures can be combined to guide toolbox users to objectively classify their data according to quality, for example to exclude or downweight poor-quality data of individuals in a statistical group analysis.

Spatial processing pitfalls. Since spatial processing in the hMRI-toolbox is embedded in the SPM framework, it is subject to the same limitations as any typical VBM study, including spatial normalisation accuracy, segmentation errors and partial volume effects (Ashburner and Friston 2000; Ridgway et al. 2008; Focke et al. 2011). Auto-reorient is an option that can help improve the segmentation.

However, it has to be done carefully. Poor signal-to-noise ratio, contrast-to-noise ratio, or outliers in the MPM input images may impair the reorientation procedure. In general, it is good practice to visually inspect the results of the hMRI pipeline to detect any obviously suspicious result. Piloting the processing pipeline using a batch for a single subject dataset is recommended, combined with a careful check of the log files (in `Results/Supplementary` and metadata including summary description as shown in Table 4).

To reduce residual misalignment (originating from the limited spatial normalisation accuracy) while preserving the quantitative nature of the MPM metrics, the hMRI-toolbox provides a dedicated smoothing approach (Fig. 4). The choice of the appropriate smoothing kernel and its performance compared to alternative methods (e.g. TBSS (Smith et al. 2006) or TSPOON (Lee et al. 2009)) is still a subject of active research.

hMRI-toolbox for different MRI scanner platforms. The first task for interested users of the hMRI-toolbox is the setup of the MPM acquisition protocol. A set of example protocols for the customised MPM as well as standard sequences available on Siemens platforms are provided on the <http://hmri.info> website. Most MPM studies up to now were carried out on Siemens MRI scanners using customised MPM sequences. Consequently, the toolbox is optimised for this vendor and MR sequences. New issues might arise when implementing the MPM protocol and using data from other vendors or conventional product sequences. For instance, different MT pre-pulse implementations will lead to changes of the MT saturation map, which will require appropriate inter-scanner calibration (Volz et al. 2010; Seif et al. 2018). Moreover, not every DICOM to NIfTI conversion software appropriately handles image intensity scaling as reported, e.g., for Philips data (Chenevert et al. 2014), leading to spurious intensity differences affecting the quantification.

Future directions. The hMRI-toolbox has been developed as a scientific collaborative project. As such its developments aim at making it broadly available, capitalising on its flexible and open-source implementation.

In terms of broad applicability of the toolbox, we aim at handling multi-scanner and multi-vendor data sets, which will require adjustments. Multi-platform applicability is facilitated for MPM protocols, since they primarily rely on multi-echo spoiled gradient echo sequences available on all modern MRI scanners (see protocol examples at <http://hmri.info>). The MPM framework together with the hMRI toolbox will be used in a multi-site clinical trial (NISCI trial, (Seif et al. 2018)) including Philips and Siemens MR systems. Even though the experience with implementing the specific MPM protocol on the Philips platforms is limited, first important steps have been achieved (Lee, Callaghan, and Nagy 2017; Lee et al. 2018) thanks to the commonly available sequences constituting the backbone of the MPM protocol. Making the hMRI-toolbox data formats fully BIDS compliant (Gorgolewski et al. 2016) by defining the ontology of acquisition parameters necessary for the creation of the quantitative maps (see B.5) further supports the use on multiple platforms and vendors, and is a high priority of the ongoing developments.

Broad applicability also involves ultra-high field MR systems. With the fast progress of ultra-high field scanners (7T and higher) on the MRI market, high-resolution data will become more routinely available and provide access to e.g. laminar-specific information (see 400 μm new generation MPM, Trampel et al. 2017), while also posing new challenges (e.g. B_1^+ field inhomogeneities) that the hMRI-toolbox will have to address.

Sensitivity to small inter-individual (e.g. developmental, see <https://www.biorxiv.org/content/early/2018/05/23/328146>) and intra-individual (e.g. plasticity) microstructural changes is another coming challenge. To that end, the bias of the qMRI estimates in the presence of motion has been investigated (Weiskopf et al. 2014; Callaghan et al. 2015a; Castella et al. 2018). Retrospective robust estimation of R_2^* parameters have been suggested in Weiskopf et al. 2014 and

could be implemented in future releases of the hMRI toolbox. Robustness must also be considered in parallel to the spatial resolution *versus* sufficient SNR level tradeoff to improve the sensitivity of the technique to small developmental changes and plasticity. Thus, spatially adaptive noise removal methods (Tabelow et al. 2016) along with appropriate handling of the Rician bias problem (Polzehl and Tabelow 2016; Tabelow et al. 2017) are important future improvements of the hMRI-toolbox.

Extensions of the hMRI-toolbox can easily fit within its modular implementation. As short term future additions, the following three modules and extensions are considered. An additional module that efficiently calculates the protocol-specific correction parameters required to account for imperfect spoiling (A.5) is planned. Quantitative susceptibility mapping (QSM), taking advantage of the existing phase images acquired with the MPM protocol (Acosta-Cabronero and Callaghan 2017; Acosta-Cabronero et al. 2018), is a second extension. Finally, adding new biophysical models that take advantage of the multi-contrast MPM data for *in vivo* histology is another priority of further developments. An example for such a direct extension of the hMRI-toolbox could be the MR g-ratio model (Stikov et al. 2015; Mohammadi et al. 2015; Ellerbrock and Mohammadi 2018). The MR g-ratio (the ratio between inner and outer diameter of a myelinated axon) is a geometrical microstructural tissue property that can be derived by combining myelin-sensitive qMRI maps from the hMRI-toolbox (e.g. *MT* or *PD* maps) with the axonal-sensitive maps obtained with existing SPM tools (e.g. the ACID toolbox (Mohammadi et al. 2012; Tabelow et al. 2015; Ruthotto et al. 2013; Mohammadi et al. 2014) and the DTI & Fiber tools (Reisert et al. 2013)).

Conclusion. The hMRI-toolbox is a highly flexible software package that provides a time-efficient, robust and simple framework to generate and process qMRI parameter maps sensitive to myelin, iron, and water content. It profits from the powerful and easy-to-use spatial and statistical analysis tools in SPM, and can be readily combined with existing SPM tools for quantitative estimation of parameter maps sensitive to complementary information such as axonal properties. The ongoing developments address the use of open-science data formats and extensions into biophysical models for direct microstructure mapping. As such, the hMRI-toolbox is one of the most comprehensive tools for estimating and processing qMRI data for neuroscience and clinical research.

ACKNOWLEDGEMENTS

EB received funding from the European Structural and Investment Fund / European Regional Development Fund & the Belgian Walloon Government, project BIOMED-HUB (programme 2014-2020). NW received funding from the European Research Council under the European Union's Seventh Framework Programme (FP7/2007-2013) / ERC grant agreement n° 616905, from the European Union's Horizon 2020 research and innovation programme under the grant agreement No 681094, and is supported by the Swiss State Secretariat for Education, Research and Innovation (SERI) under contract number 15.0137. SM was supported by the Deutsche Forschungsgemeinschaft, grant MO 2397/4-1. NW and SM received funding from the BMBF (01EW1711A and B) in the framework of ERA-NET NEURON. BD is supported by the Swiss National Science Foundation (NCCR Synapsy, project grant Nr 32003B_159780) and Leenaards Foundation. AL is supported by the Roger De Spoelberch Foundation. LREN is very grateful to the Roger De Spoelberch and Partridge Foundations for their generous financial support. MFC is supported by the MRC and Spinal Research Charity through the ERA-NET Neuron joint call (MR/R000050/1). The Wellcome Centre for Human Neuroimaging is supported by core funding from the Wellcome [203147/Z/16/Z]. CP is supported by the F.R.S.-FNRS, Belgium. LR's work was supported by a grant from Emory University's Research Council. GH was funded by the Swedish Research Council NT 2014-6193. The authors thank Sanne Kikkert at ETH Zurich for helpful comments on the manuscript. Evelyne Balteau, Karsten Tabelow and Siawoosh Mohammadi contributed equally to this paper.

APPENDIX A. SUMMARY OF THE MODEL FOR MPM

A.1. R_1 and PD estimation. For a single excitation and echo time TE , the signal intensity S is given by the Ernst equation for an ideal spoiled gradient echo acquisition (Ernst and Anderson 1966; Helms, Dathe, and Dechent 2008):

$$(1) \quad S = A \cdot \sin \alpha \cdot \frac{1 - e^{-R_1 \cdot TR}}{1 - \cos \alpha \cdot e^{-R_1 \cdot TR}} \cdot e^{-R_2^* \cdot TE}.$$

We denote the repetition time by TR and the flip angle by α . A is proportional to the equilibrium magnetisation and thus to the proton density PD (Helms, Dathe, and Dechent 2008).

For fast estimation of the R_1 and A parameters from (1) and a single echo of a T1w and a PDw acquisition, or the mean across multiple echoes for increased SNR, Helms, Dathe, and Dechent 2008 introduced a linearisation of its exponential terms for short TR (i.e. $R_1 \cdot TR \ll 1$):

$$(2) \quad e^{-R_1 \cdot TR} \simeq 1 - R_1 \cdot TR$$

leading to, after averaging over echos,

$$(3) \quad S \simeq A^* \cdot \sin \alpha \cdot \frac{R_1 \cdot TR}{1 - \cos \alpha \cdot (1 - R_1 \cdot TR)}$$

with

$$(4) \quad A^* = \frac{A}{\#echoes} \cdot \sum_{TE} e^{-R_2^* \cdot TE}$$

When S is the averaged signal over several echoes, the sum in Eq. (4) is calculated across all echoes included in the averaged signal. This introduces an R_2^* bias which increases with the number of echoes and depends on the TE values included in the average. The R_2^* bias in A^* can be evaluated using the R_2^* estimate and corrected for. Alternatively, S can be the extrapolated signal at $TE = 0$, which is free from R_2^* weighting. Both the echo averaging with R_2^* correction method and the $TE = 0$ extrapolation method are implemented and available in the toolbox, and perform similarly (Balteau et al. 2018). The toolbox extrapolates to a TE of 0 ms by default.

Using the approximation $\sin(\alpha) \simeq \alpha$ and $\cos(\alpha) \simeq 1 - \alpha^2/2$ for small flip angles and neglecting the term $\alpha^2 \cdot R_1 \cdot TR$, Eq. (1) simplifies to:

$$(5) \quad S = A^* \cdot \alpha \cdot \frac{R_1 \cdot TR}{\alpha^2/2 + R_1 \cdot TR}$$

from which R_1 and A^* are estimated using the signals from the PDw and T1w sequences:

$$(6) \quad R_1 \simeq \frac{S_{PD} \alpha_{PD} / TR_{PD} - S_{T1} \alpha_{T1} / TR_{T1}}{2 \cdot (S_{T1} / \alpha_{T1} - S_{PD} / \alpha_{PD})}$$

$$(7) \quad A^* \simeq \frac{S_{T1} S_{PD} (TR_{T1} \alpha_{PD} / \alpha_{T1} - TR_{PD} \alpha_{T1} / \alpha_{PD})}{S_{PD} TR_{T1} \alpha_{PD} - S_{T1} TR_{PD} \alpha_{T1}}$$

where signals S_{T1} and S_{PD} are either averaged over a number of echoes (Helms, Dathe, and Dechent 2008), or extrapolated to $TE = 0$, as explained above. In the first case, a $\sum_{TE} e^{-R_2^* \cdot TE}$ correction factor must be calculated to derive A (Balteau et al. 2018). $A = A^*$ otherwise meaning that the R_2^* bias remains.

A.2. Estimation of the magnetisation transfer. The MT (magnetisation transfer) saturation measure is derived in analogy to a dual-excitation spoiled gradient echo sequence where the second

excitation is replaced by the MT pulse. Using a heuristic approximation, the closed form solution for the acquired signal S can be written (Helms and Hagberg 2009; Helms et al. 2008) as

$$(8) \quad S = A \cdot \sin \alpha_{MT} \cdot \frac{1 - e^{-R_1 \cdot TR_{MT}} - \delta \cdot (e^{-R_1 \cdot TR_2} - e^{-R_1 \cdot TR_{MT}})}{1 - \cos \alpha_{MT} \cdot (1 - \delta) \cdot e^{-R_1 \cdot TR_{MT}}} \cdot e^{-R_2^* \cdot TE}$$

where $TR_{MT} = TR_1 + TR_2$ is the total repetition time, α_{MT} is the on-resonance flip angle of the MTw sequence and δ describes the MT saturation (more generally denoted MT in this paper).

From an additional MTw signal S_{MT} we obtain, using again the linearisation of the exponential term for short TR_{MT} (i.e. $R_1 \cdot TR_{MT} \ll 1$) and the small angle approximation for the trigonometric functions:

$$(9) \quad \delta = MT = (A^* \alpha_{MT} / S_{MT} - 1) \cdot R_1 \cdot TR_{MT} - \alpha_{MT}^2 / 2$$

see Helms et al. 2008. Note that the parameter maps R_1 , R_2^* , A and MT can alternatively be estimated from the ESTATICS model using analytic formulas and not relying on the linearisation outlined above (Tabelow et al. 2016).

A.3. The ESTATICS model and R_2^* estimation. The ESTATICS model was introduced in Weiskopf et al. 2014 for efficiently estimating the effective transverse relaxation rate R_2^* from an MPM acquisition protocol, where the exponential signal decay with the echo time is identical for T1w, PDw and MTw acquisitions. Specifically, the signal equations (1) and (8) are re-written as

$$(10) \quad S = (S_{PD} \cdot I_{PD} + S_{T1} \cdot I_{T1} + S_{MT} \cdot I_{MT}) \cdot e^{-R_2^* \cdot TE}$$

with indicator variables I_{PD} , I_{T1} , and I_{MT} for the differently weighted acquisitions. The signal intensities, e.g. S_{PD} , at $TE = 0$ are given by

$$(11) \quad S_{PD} = A \cdot \sin \alpha_{PD} \cdot \frac{R_1 \cdot TR_{PD}}{1 - \cos \alpha_{PD} (1 - R_1 \cdot TR_{PD})}$$

with the flip angle and repetition time of the PDw sequence and correspondingly for S_{T1} and S_{MT} . From Eq. (10) R_2^* can be estimated using all echoes.

A.4. Corrections for transmit and receive field inhomogeneities. Due to inhomogeneities of the B_1 transmit field the local flip angle deviates from its nominal value (Helms, Dathe, and Dechent 2008). Using a correction field f_T , the effective local flip angle is given by

$$(12) \quad \alpha_{corr} = f_T \cdot \alpha$$

For details on the correction field f_T estimation see Section 3.7.2 and C.3.

For the MTw acquisition we denote by α_{sat} the off-resonance Gaussian shaped RF pulse used for MT weighting. The B_1 transmit bias field $f_T(x)$ leads to a local correction of α_{sat} , too, and thus to a residual bias field for the estimated δ even though δ is largely independent of the local transmit field bias unlike other MT metrics such as MTR (Helms et al. 2008; Callaghan et al. 2014) In Helms 2015 the heuristic correction factor for δ was found to be

$$(13) \quad \frac{1 - B \cdot \alpha_{sat}}{(1 - B \cdot f_T \cdot \alpha_{sat}) \cdot f_T^2}$$

with $B \cdot \alpha_{sat} = 0.4$ for the typically used value $\alpha_{sat} = 220^\circ$ in MPM sequences (Weiskopf et al. 2013).

Finally, the multiplicative RF sensitivity bias field f_R (see Section 3.7.3 and C.4) for the correction of the signal amplitude maps A :

$$(14) \quad A_{corr} = A \cdot f_R$$

has to be measured or estimated from the data (for details see section 3.7.3). The A^* maps can then be normalised to proton density PD maps by calibration. To this end, the mean PD value in white matter is assumed to be 69 percent units (p.u.) (Tofts 2003).

A.5. Spoiling corrections. Further, imperfect spoiling requires an additional correction when estimating R_1 (Preibisch and Deichmann 2009), to account for deviation from Ernst equation (1). The correction is performed using the following expression

$$(15) \quad R_1^{corr} = \frac{R_1}{P_a(f_T) \cdot R_1 + P_b(f_T)}$$

where $P_a(f_T)$ and $P_b(f_T)$ are quadratic functions in f_T . Their coefficients depend on the specific sequence and can be determined by simulation (Preibisch and Deichmann 2009). Further refinements of this correction include diffusion effects on signal spoiling (Yarnykh 2007; Lutti and Weiskopf 2013; Callaghan, Malik, and Weiskopf 2015).

APPENDIX B. DICOM IMPORT AND JSON METADATA

To support the flexibility of the hMRI processing pipeline and the traceability of the data at every step, a number of parameters from acquisition to statistical results must be retrieved and stored.

Therefore, DICOM import and JSON metadata handling functionalities have been implemented with the following objectives:

- 1 retrieving the full DICOM header as a readable and searchable Matlab structure (metadata),
- 2 during DICOM to NIfTI conversion, storing the metadata structure as separate JSON file (alongside the NIfTI image file) and/or as extended header into the NIfTI image file,
- 3 handling metadata in order to set, get and search parameters.

With the current implementation, these objectives are achieved: the hMRI-toolbox handles and stores data acquisition and processing parameters as JSON-encoded metadata alongside brain imaging data sets. The implementation rests on the SPM12 implementation of DICOM tools (`spm_dicom_header(s)`, `spm_dicom_essentials`, `spm_dicom_convert`) and relies on `spm_jsonread` and `spm_jsonwrite` for handling JSON-encoded metadata.

From SPM12 version r7219 (released 16 November 2017) and in later versions, functionalities described at points 1. and 2. above (excluding the extended header option though) have been integrated to the DICOM import module in SPM12 (implementation from the hMRI-toolbox). Note that some features of the hMRI-toolbox metadata library (for metadata handling, in particular to set, get and search the metadata) are not available in the SPM12 distribution.

Detailed syntax and many examples are provided in the hMRI-toolbox Wiki, we briefly describe the main features and the metadata structure below.

B.1. DICOM to NIfTI conversion. The `spm_dicom_convert` script has been modified to achieve the above goals. An additional input argument has been set to deal with the new JSON metadata options. If JSON metadata storage is enabled, DICOM header information is stored as a JSON-formatted structure either as a separate JSON file or as extended NIfTI header (or both). If omitted or disabled, the DICOM to NIfTI conversion proceeds using exactly the same implementation as in the previously mentioned SPM12 distribution. The output NIfTI images, extended or not, have a valid NIfTI-1 format compatible with standard NIfTI readers (MRICron, SPM, FreeSurfer). Note that FSL up to version v5.0.9 does not support extended headers. For that reason, the extended header option, although suggested in (Gorgolewski et al. 2016) is currently not recommended and disabled by default. Instead, a separate JSON file is created.

B.2. DICOM to NIfTI conversion – SPM Batch. The DICOM to NIfTI conversion with the above features is available through the hMRI-toolbox in the SPM Batch GUI (SPM > Tools > hMRI Tools > DICOM Import). The new JSON metadata format field provides the user with the following options:

- None
- Separate JSON file (default)
- Extended nii header
- Both

B.3. The metadata structure. Metadata are simple MATLAB structures, hence quite flexible and modular. The structure of the metadata is divided into the following two main fields:

- **Acquisition parameters (hdr.acqpar):** this branch contains the *original DICOM header*. It should be kept unchanged and is created when importing DICOM images to NIfTI. It is dropped for processed images relying on several input images.
- **History (hdr.history):** is a *nested* structure containing
 - **procstep:** a structure describing the current processing step and containing:
 - **descrip:** a brief description of the processing applied (e.g. DICOM to NIfTI conversion, realign, create map, ...)
 - **version:** version number of the processing applied, for traceability
 - **procpar:** processing parameters (relevant parameters used to process the data – e.g. for SPM processing, all the settings included in the MATLAB batch job except for the input images).
 - **input:** An array listing the input images used for the processing. Each input (hdr.history.input(i)) is a structure containing:
 - **filename:** the filename of the input image
 - **history:** the history structure from the input image
 - **output:** a structure containing
 - **imtype:** image type of the current output (e.g. R_1 , FA , MT , ADC) including a summary description of the processing steps (see Table 4).
 - **units:** either physical units (sec, 1/sec, ...), standardised units (e.g. percent units = p.u.) or arbitrary units (a.u.).

B.4. Metadata handling. The JSON transcription of the MATLAB structure is easily readable and searchable by opening the extended NIfTI or separate JSON file with a text editor. Furthermore, metadata set, get and search tools have been implemented. These tools have been added into the spm12/metadata directory. Typing `help <function>` in MATLAB gives detailed syntax. Below is a list of the most useful scripts and their summary descriptions. For a complete description of the implemented tools, please refer to the hMRI-toolbox Wiki pages.

`get_metadata`: returns the MATLAB structure described above.

`set_metadata`: to write (insert, modify, overwrite) metadata in JSON files and extended NIfTI headers. In general, metadata are initialised during the DICOM to NIfTI conversion and further modified as the processing progresses.

`get_metadata_val`: returns pairs of structure fields and values agreeing with search criteria.

`find_field_name`: recursively searches a MATLAB structure for a specific field name (can be applied to any MATLAB structure).

Output map	metadata.history.output.imtype
(A) $R_{1,Ref}$	R1 map [s-1] - B1+ bias correction using provided B1 map (i3D_EPI) - RF sensitivity bias correction based on a per-contrast sensitivity measurement
(B) $R_{1,UNICORT}$	R1 map [s-1] - B1+ bias correction using UNICORT - RF sensitivity bias correction based on a per-contrast sensitivity measurement
(C) $R_{1,None}$	R1 map [s-1] - no B1+ bias correction applied - RF sensitivity bias correction based on a per-contrast sensitivity measurement

TABLE 4. JSON Metadata example: Metadata are stored as a Matlab structure in the JSON file associated to each output (NIfTI) image. The metadata structure can easily be retrieved using the following SPM/Matlab command: `metadata = spm_jsonread(<name of the JSON file>)`. The structure includes processing parameters, dependencies of the result on other input images as well as a summary description of each output image. As an example, the image type of each output R_1 image used to generate Figure 6 is provided in the Table. The highlighted lines (bold font) describe the B_1 transmit bias correction, illustrating the user-friendly traceability of the processing steps used to generate an image. The same information can be read directly from the JSON file using a text editor.

B.5. General usage of the metadata and BIDS compatibility. The DICOM import with metadata storage is now available in the SPM distribution (SPM12.4 - r7219) allowing for a wide use of such metadata. It provides most of the parameters required for map creation and processing. The hMRI-toolbox also provides metadata handling functionalities to retrieve parameter values and store processing parameters in the JSON-encoded metadata file. The format used for the metadata provides flexibility for using a wide range of protocols, and traceability of every parameter used to generate the results (see for example Table 4).

Outside the hMRI-toolbox, metadata and metadata handling tools implemented in the hMRI-toolbox can prove useful for many purposes. For quality control, metadata can help checking for protocol consistency by comparing essential parameters across sessions, subjects and sites. When processing data acquired with several protocols on several scanners from different vendors (multicentric studies), metadata provide the information to automatically extract acquisition parameters to be used as regressors of no interest in a statistical analysis (e.g. MR scanner, field strength, head coil, ...). Metadata also facilitate the sorting of the data between different data types (e.g. functional MRI, structural MRI, diffusion images, etc.) together with retrieving BIDS essential parameters (e.g. repetition time, echo time, flip angle, session and series numbers, etc.), therefore providing all the information required to make the data archiving and storage fully BIDS-compatible.

A *BIDS extension proposal (BEP)* is currently under discussion, that will define the parameters necessary to describe *structural acquisitions with multiple contrasts* (see <https://bids.neuroimaging.io/> for updates on BIDS specifications and extension proposals), and bring the metadata structure of such data in line with the BIDS recommendations (Gorgolewski et al. 2016). The extension will include all acquisition parameters required to fully describe and process data acquired with the MPM protocols, in a standard, platform- and vendor-independent way. With such BIDS extension, the hMRI-toolbox will be adapted and made fully BIDS-compliant, from the structure of the JSON-encoded metadata

to the structure of the output data. The required adaptation will be achieved smoothly thanks to the metadata handling functionalities, without affecting the processing part of the hMRI-toolbox.

APPENDIX C. DETAILED DESCRIPTION OF THE hMRI MODULES

C.1. *Configure toolbox module.* The *Configure toolbox* module must be run before any other module for the default parameters to take effect.

The default settings are defined and described in the `config` directory. The default files therein should never be modified. Template files for customised default parameters are stored in the `config/local` directory and can be modified and saved with meaningful names by the user. Note that most parameters should only be modified by advanced users who are aware of the underlying theory and implementation of the toolbox.

For brevity, a full description of each customisable setting is not provided here. A detailed description of each parameter may be found in the `hmri_local_defaults.m` help and examples are provided in the toolbox Wiki pages. Note that the default settings for B_1 transmit bias correction (also including acquisition and processing parameters) can be customised separately within the *Create hMRI maps* module (C.3). Their customisation must follow the same guidelines as provided in this section.

While settings need to be defined either in the standard or customised default files, acquisition parameters can be retrieved from the input images if included in the metadata. When no metadata are available or not yet properly handled by the toolbox (e.g. customised sequences), acquisition parameters specified in the default files are used as a fallback solution. The use of metadata is strongly recommended (see B), to automatically retrieve acquisition parameters and to avoid incorrect processing.

C.2. *Auto-reorient module.* This module performs a rigid-body alignment of a subject's structural image into the MNI space, applying the estimated pose to a set of *other images*. The code makes use of the `spm_affreg` function and *canonical* images available in SPM12. The user must provide one structural image from the subject and a corresponding canonical image for co-registration, and a series of other images that need to be kept in alignment with the structural image (typically, all the images acquired during a given imaging session). The structural image should have good signal-to-noise ratio with a high white matter/grey matter contrast-to-noise to ensure a robust and reliable co-registration. The SPM canonical images can be selected from the `SPM/canonical` directory or any other user-defined template (e.g. atypical population-driven template), provided it is already oriented according to MNI. Since the registration is based on matching similar intensities, it is important that the contrast of the reference image be close to that of the canonical image. The following list is provided as guidelines:

Source image	Recommended template
First T1w echo	SPM/canonical/avg152T1.nii
First PDw echo	SPM/canonical/avg152PD.nii
First MTw echo	SPM/canonical/avg152PD.nii

If no specific output directory is selected, the original orientation of the images will be overwritten. If an output directory is selected then the images are copied there before being reoriented, therefore leaving the original data untouched. The reoriented images can be collected as dependencies for further processing in the batch interface, either all at once (`Dependencies > Grouped`) or as individual output images (`Dependencies > Individual`), which is more convenient to connect the *Auto-reorient* module to the next *Create hMRI maps* module.

C.3. B_1 transmit field corrections. Within the *Create hMRI maps* module, several methods for B_1 transmit field correction are implemented. Depending on the choice of the specific method the GUI requires the user to provide adequate input files, which are described below. In order to proceed to the B_1 map calculation, number of acquisition parameters must also be either retrieved from the metadata or provided to the toolbox via a standard or customised default B_1 file (see below and in C.1).

1 `3D_EPI`

EPI spin-echo (SE)/stimulated-echo (STE) method (Lutti, Hutton, and Weiskopf 2009; Lutti et al. 2012).

The sequence uses a set of pulses with nominal flip angles α , $2 \cdot \alpha$ and α to create pairs of spin echo and stimulated echo images. All consecutive pairs of SE/STE images corresponding to the different nominal flip angle values α of the SE/STE RF pulse must be loaded as `B1 input`. B_0 field mapping images must also be provided for correcting distortions in the EPI images. Both magnitude images and the pre-subtracted phase image must be selected, in that order, as `B0 input`.

2 `3D_AFI`

Actual Flip Angle Imaging (AFI) method (Yarnykh 2007).

A pair of magnitude images acquired with two different repetition times (TR) must be loaded as `B1 input`. The hMRI-toolbox then calculates the B_1 transmit bias field map as described in Yarnykh 2007.

3 `tfl_b1_map`

TFL B_1 mapping (Chung et al. 2010).

For this method, the batch interface requests a pair of images (one anatomical image and one flip angle map, in that order) from a service sequence by Siemens (version available from VE11 on) based on a turbo flash (TFL) sequence with and without a pre-saturation pulse (Chung et al. 2010). The flip angle map used as input contains the measured flip angle multiplied by 10. After rescaling (p.u.) and smoothing, the output f_T map is ready to be used for B_1 transmit bias correction.

4 `rf_map`

This requires a pair of images (one anatomical image and one pre-processed B_1 map, in that order) from a service sequence by Siemens (Erlangen, Germany). These are based on the acquisition of a spin-echo/stimulated echo as used for method `3D_EPI` above (Lutti, Hutton, and Weiskopf 2009; Lutti et al. 2012). Rescaling and smoothing is applied to the input B_1 map (a.u.) to generate a f_T map (p.u.) suitable for B_1 transmit bias correction.

5 `pre-processed B1`

Any B_1 transmit bias field map pre-calculated using one of the above methods or another method can be used as pre-processed `B1 input`. The user must select one anatomical reference (for co-registration) and one B_1 map (in p.u.), in that order. The anatomical reference is typically a magnitude image from the B_1 mapping dataset, and must be in the same space as the B_1 transmit bias field map.

6 `UNICORT`

Data driven estimation of the B_1 transmit bias field map using the UNICORT approach (Weiskopf et al. 2011).

If none of the above mentioned methods applies because no appropriate B_1 transmit bias field mapping data were acquired, the UNICORT option is recommended to remove the transmit field bias in the R_1 map and estimate the B_1 transmit bias field map from the qMRI data. Optimal UNICORT processing parameters are RF transmit coil dependant. The default parameters have been optimised for Siemens 3T TIM Trio scanners and may need specific optimisation for other RF transmit coils. See the hMRI-toolbox Wiki for guidelines.

7 `no_B1_correction`

With this option, no correction for transmit inhomogeneities is applied, i.e. $f_T \equiv 1$.

For each B_1 mapping protocol (1-4), one `*_B1map` (in p.u.) and one `*_B1ref` (for anatomical reference) file is created and saved in the `Results/Supplementary` directory (see Table 3). The output images are associated with JSON metadata including the type of B_1 map processed and the setting used. For UNICORT, only the `*_B1map` in p.u. is created (in the same space as the qMRI maps) with no anatomical reference. For pre-processed B_1 transmit bias field maps provided by the user, the input files are not renamed to match the naming convention above. Default acquisition and processing parameters for the UNICORT, 3D_EPI and 3D_AFI methods can be customised at this point by providing the `Create hMRI maps` module with a customised configuration file (see C.1 and the hMRI Wiki pages for guidelines). Except for UNICORT, where the B_1 transmit bias field is directly derived from the qMRI data, and the `no_B1_correction` option, where no anatomical reference is given, the hMRI-toolbox co-registers the anatomical reference image with the multi-echo spoiled gradient echo data before applying the B_1 transmit bias correction.

C.4. Receive (RF) sensitivity bias correction. In this paragraph, the RF sensitivity bias correction methods based on measured RF sensitivity maps (`Single` or `Per contrast` options) as well as the data driven method (`Unified Segmentation` option: no input sensitivity map required) will be explained in detail.

Receive field sensitivity measurements. Since the receive field sensitivity of the body coil is assumed to be flat over the spatial extent of the head (Pruessmann et al. 1999), if the same anatomy is imaged with the head coil and the body coil sequentially, using the same acquisition parameters and assuming no motion, then the ratio of these two scans is proportional to the net head coil receive sensitivity field f_R :

$$(16) \quad S_{HC} = f_R S_0; S_{BC} = C_{BC} S_0$$

$$(17) \quad S_{HC}/S_{BC} = f_R/C_{BC}$$

where S_{HC} is the signal acquired with the head coil, f_R is the receive sensitivity field of the head coil, S_{BC} is the same signal acquired by the body coil, C_{BC} is the receive sensitivity field of the body coil assumed to be approximately constant, and S_0 is the signal specific to the underlying anatomy and acquisition parameters.

If receive field sensitivity measurements are available for each imaging contrast (one receive sensitivity field acquired either before or after each of the PDw, T1w and MTw contrasts), inter-scan variation of the sensitivity modulation can be accounted for and used to optimally correct for the combined inter-scan motion and sensitivity modulation effects in the quantitative maps (Papp et al. 2016 and Figure 5a). Therefore, the implemented RF sensitivity correction method (`Per contrast` option) combines a correction for motion-related relative receive sensitivity variations with rigid-body realignment.

The low resolution measurements from the head and body coils (in this order) for each T1w, PDw and MTw acquisition are expected as inputs to the RF sensitivity bias correction. A receive field sensitivity map is calculated according to Eqs. 16 and 17 for each contrast, and applied to the corresponding contrast to correct for any coil sensitivity driven signal intensity modulation.

If RF sensitivity measurements are missing for some of the contrasts, or if only one single measurement is available, the same RF sensitivity bias correction can still be applied to all contrasts by choosing the corresponding (`Single`) option in the GUI. Only one pair of head coil and body coil images is required. Receiver field inhomogeneities will be corrected for although not accounting for inter-scan motion (Figure 5b-d). Note that the measured RF sensitivity maps are modulated by the receive field of the body coil, which is not corrected for (Figure 5e).

Data driven receive field estimation. If no receive field sensitivity map has been acquired, the `Unified Segmentation` option can be selected in the GUI. The receive field bias is then estimated from the calculated A map using SPM unified segmentation (US) approach (Ashburner and Friston 2005). Accurate bias field estimation requires the use of a brain mask combining the white and grey matter probability maps. The latter are derived by segmentation of the calculated MT map (because of its higher contrast in the basal ganglia, see Helms et al. 2009) or alternatively (if no MT images are available), by segmentation of the calculated R_1 map. The optimal US parameters depend on the RF receive coil and its sensitivity profile. Fine adjustment of the US parameters might be required for a specific RF receive coil.

C.5. Process hMRI maps module. This section describes the three main operational steps of the spatial processing pipeline for hMRI data: segmentation, diffeomorphic registration and tissue-weighted smoothing. Furthermore, it provides details on the fully integrated processing pipeline, which is proposed in this toolbox as a separate sub-module to facilitate standard spatial data processing without the need to combine the individual steps.

The processing tools and user interface can be used to process parameter maps generated from a series of subjects, assuming that each subject has the same small number of images (for example the four MT , PD , R_1 , and R_2^* maps). Therefore each module takes as input several series of images sorted per image type (for example the MT from all the subjects). The images in each series must follow the same subject-based ordering.

C.5.1. Segmentation. This step relies on the latest unified segmentation (US) algorithm as available in SPM12 (Ashburner and Friston 2005) and is interfaced through a single module. Compared to the *SPM12-Segment* module, the *hMRI-Segment* module allows the successive processing of a series of subjects.

The segmentation itself relies on one structural image per subject, typically an MT map, R_1 map or T1w image, and a set of tissue probability maps (TPMs). The TPMs used by default in the *hMRI-toolbox* were specifically derived from multi-parametric maps (Lorio et al. 2014) denoted as *extended TPMs* (eTPM).

By default (adjustable in the batch interface), the segmentation step generates a series of tissue class images in native space: the `c1/c2/c3` images - for gray matter (GM), white matter (WM) and CSF, as well as Dartel-imported `rc1/rc2` images. The segmentation module also outputs the GM and WM tissue class images warped into MNI space (classic elastic deformation, i.e. *not* with Dartel) with (`wmc1/wmc2` images) and without (`wc1/wc2` images) Jacobian modulation. Finally, the estimated segmentation and deformation fields are available as a `.mat` file and 4D `y_* .nii` files respectively. See the upper part of Table 5 for a complete file list and description of the output.

C.5.2. Diffeomorphic registration. This step includes three sub-modules derived from the Dartel toolbox (Ashburner 2007). The key idea of Dartel is to iteratively align the tissue class images, typically the grey and white matter, from a series of subjects to their own average, i.e. one per tissue class considered, by generating successive mean images with higher overlap and detail (called ‘Templates’). This only depends on the Dartel-imported tissue class images from each subject.

The three sub-modules included are as follows:

Run Dartel, create Templates. This module aligns together tissue class images from the series of subjects. In addition a set of Templates (population average tissue class images, with increasing sharpness), this sub-module creates a deformation field for each subject, which encodes the nonlinear alignment with the final template. See the second part of Table 5.

File name	Description
<i>Unified Segmentation (US)</i> (Proc. hMRI -> Segmentation)	
c1<segmInputFileName>.[nii json]	Tissue class 1 in subject space. Prefixes c1/c2/c3 correspond to GM/WM/CSF respectively.
rc1<segmInputFileName>.[nii json]	Tissue class 1 in subject space, resliced and imported for Dartel processing. Dartel usually relies on rc1/rc2 images (GM/WM) only.
wc1<segmInputFileName>.[nii json]	Tissue class 1 warped into MNI space, with the simple warp obtained with the <i>US</i> . Prefixes w1/wc2 correspond to GM/WM respectively.
mw1<segmInputFileName>.[nii json]	Tissue class 1 warped into MNI space, with the simple warp obtained with the <i>US</i> , and modulated by the determinant of the Jacobian, i.e. accounting for local change of volume. Prefixes mw1/mw2 correspond to GM/WM respectively.
y_<segmInputFileName>.nii	Deformation field, i.e. warps, obtained from <i>US</i>
<segmInputFileName>_seg8.mat	Segmentation and warping parameters, obtained from <i>US</i>
<i>Diffeomorphic registration</i> (Proc. hMRI -> Dartel -> Run Dartel (create Templates))	
u_rc1*_Template.nii	Flow field image, one per subject, estimated by Dartel from the rc1/rc2 images.
Template_*.nii	7 template images, numbered from 0 to 6, created by Dartel from the rc1/rc2 images of all the subjects.
<i>Diffeomorphic registration</i> (Proc. hMRI -> Dartel -> Normalise to MNI space)	
w*<normInputFileName>.[nii json]	Image warped into MNI space following Dartel, using the estimated <i>flow field</i> and an affine transformation. This would be typically a qMRI map that should <i>not</i> be modulated to account for volume changes.
mw*<normInputFileName>.[nii json]	Image warped into MNI space and modulated by the determinant of the Jacobian, i.e. accounting for local change of volume. This would typically be any tissue probability map (i.e. image with a measure whose total amount over the brain volume should be preserved) to be used after smoothing for a VBM analysis.
<i>Tissue-weighted smoothing</i> (Proc. hMRI -> Smoothing)	
wap1_<smooFileName>.[nii json]	Tissue-weighted smoothing for tissue class 1.
s*<FileName>.[nii json]	(Any) image smoothed with a standard Gaussian filter (here for comparison, <i>not</i> in hMRI).

TABLE 5. Output files from the *Process hMRI maps* modules. The file names are based on the file name of the map or image used as input to the Segmentation, Dartel > Run Dartel (create Templates), Dartel > Normalise to MNI space, and Smoothing steps. Note that wc*<InputFileName>.[nii|json] images can be obtained either with the simple warp obtained with the *Unified Segmentation* or following Dartel with the Dartel > Normalise to MNI space module.

Run Dartel, existing Templates. If the set of Templates already exists, this sub-module can be used to estimate only the deformation fields for another set of new subjects (relying on the same form of tissue class images as those used to generate the Templates).

Normalize to MNI. This module applies the estimated deformation fields to the parameter maps and tissue class images, bringing them all into alignment with MNI space. Unlike to the Dartel toolbox, no smoothing is applied at this stage, but a specific smoothing operation is applied at the next *Tissue-weighted smoothing* step. See the third part of Table 5 for the file list and description.

The machinery behind those modules are exactly the same as the 'Dartel toolbox' available elsewhere in SPM. They have only been included in the hMRI-toolbox for ease of use. Moreover the user-interface of the *Normalize to MNI* module was slightly extended to more efficiently handle the multiple parameter maps and tissue class images of each subject. Notably, in contrast to many typical VBM applications, quantitative parameter values are not modulated (to account for volume changes) during this normalization.

C.5.3. *Tissue-weighted smoothing*. As proposed in Draganski et al. 2011, the parameter maps should be smoothed to improve spatial realignment while accounting for the partial volume contribution of the tissue density in each voxel in subject space. This combination of weighting and smoothing is

expressed as:

$$(18) \quad v = \frac{g * (w s(\phi)[eTPM(t) > .05])}{g * w} [g * w > .05]$$

where:

- v is the resulting *tissue-weighted smoothed* image;
- $g*$ stands for convolution with a Gaussian smoothing kernel;
- ϕ encodes the spatial deformation from subject to standard space;
- $s(\phi)$ is a parameter map (e.g. MT , R_1 ,...) in standard space warped by ϕ ;
- $w = |D\phi|t(\phi)$, the weights representing the tissue class density in standard space, accounting for volume changes;
- $t(\phi)$ represents subject's tissue class image, typically GM or WM, warped by ϕ ;
- $|D\phi|$ is a Jacobian determinants of deformation ϕ ;
- $[x > 0.05]$ is a masking operation where voxels with a value x smaller than .05 are set to zero.

The masking ensures that only voxels with a) an *a priori* probability of being in the considered tissue class above 5% (i.e. the whole intra-cranial brain volume for GM and WM) and b) original tissue density in native space above 5% are included in the resulting smoothed image.

One *tissue-weighted smoothed* map (v) is generated per tissue class (t) and parameter map (s). These images can then be statistically analysed. See the bottom part of Table 5 for the file prefix list and description. Note, that the tissue-weighted smoothed maps for different tissue classes will spatially overlap, because they were thresholded at 5%. Thus, additional masking of these tissue-specific maps at the group-level may be desirable to ensure that a given voxel is analysed only once. Also note, that the VBQ smoothing, in contrast to typical VBM analyses, does not modulate the parameter maps (to account for volume changes), but instead preserves the quantitative values of the original qMRI maps in MNI space.

C.5.4. Integrated pipeline. Spatial processing of multiple parameter maps would typically combine four modules (*Segmentation*, *Run Dartel*, *create Templates*, *Normalize to MNI*, and finally *Tissue-weighted smoothing*) into a single batch. The options of each module can be adjusted and the images passed from one module to the next via virtual dependencies, as available in the batch-GUI, forming a complete processing pipeline. An alternative approach, simpler but less spatially accurate (not recommended), would skip the diffeomorphic warping steps and only combine the *Segmentation* and *Tissue-weighted smoothing* modules.

To help novice users, an *Integrated pipeline* module directly enacts the whole procedure with minimal user input. The module only requires the following inputs:

- the series of structural reference images and parameter maps (one per subject),
- the width of the Tissue-weighted smoothing kernel desired,
- the type of processing pipeline, i.e. with or without diffeomorphic registration (Dartel).

All the other options of each of the intermediate steps are set by defaults, e.g. only GM and WM tissue classes are of interest and the TPMs are those from the `hMRI-toolbox`.

APPENDIX D. QUANTITATIVE MAPS AND QUALITY ASSESSMENT

The quality of the quantitative maps generated using the `hMRI-toolbox` can be assessed using the Quality Assessment (QA) tool. This tool is enabled via the `QA` flag in the `hmri_defaults.m`

file and can be modified using a local configuration (C.1). When enabled, a JSON-encoded MATLAB structure containing objective measures of the quality of the data is saved in the `Results/Supplementary` directory (Table 3). The structure contains the following fields:

- 1 Coregistration parameters of the MTw and T1w images to the PDw images (translation in mm and rotation in radians), providing measures of head motion between the corresponding images (*inter-scan motion*).
- 2 Standard deviation in white matter of the R_2^* maps calculated from each individual contrast. Provides measures of image degradation due to head motion during the acquisition of the corresponding image (*intra-scan motion*) (Castella et al. 2018).
- 3 Mean and standard deviation values of the signal intensity values in white matter after B_1 receive bias correction (PD map calculation). The value of the standard deviation, relative to the mean, reflects the accuracy of the bias-field correction though pathological inhomogeneities of brain tissue (e.g. brain lesions) may also contribute.

REFERENCES

- Acosta-Cabronero, J. and M. F. Callaghan (2017). “Quantitative susceptibility mapping from variable flip angle measurements”. In: *ESMRMB 2017*.
- Acosta-Cabronero, J., C. Milovic, H. Mattern, C. Tejos, O. Speck, and M. F. Callaghan (2018). “A robust multi-scale approach to quantitative susceptibility mapping”. *NeuroImage*. URL: <https://doi.org/10.1016/j.neuroimage.2018.07.065>.
- Alonso-Ortiz, E., I. R. Levesque, and G. B. Pike (2017). “Impact of magnetic susceptibility anisotropy at 3T and 7T on T2*-based myelin water fraction imaging”. *NeuroImage*. URL: <https://doi.org/10.1016/j.neuroimage.2017.09.040>.
- Ashburner, J and K. J. Friston (2000). “Voxel-based morphometry—the methods”. *NeuroImage* 11.6 Pt 1, pp. 805–821.
- Ashburner, J. (2007). “A fast diffeomorphic image registration algorithm”. *NeuroImage* 38.1, pp. 95–113.
- Ashburner, J. and K. J. Friston (2005). “Unified segmentation”. *NeuroImage* 26.3, pp. 839–851.
- Assaf, Y. and P. J. Basser (2005). “Composite hindered and restricted model of diffusion (CHARMED) MR imaging of the human brain”. *NeuroImage* 27.1, pp. 48–58.
- Balteau, E., T. Leutritz, N. Weiskopf, E. Reimer, A. Lutti, M. F. Callaghan, S. Mohammadi, and K. Tabelow (2018). “Evaluating T2* bias impact and correction strategies in quantitative proton density mapping”. In: *Proceedings of ISMRM 2018*, p. 2694.
- Baudrexel, S., S. C. Reitz, S. Hof, R.-M. Gracien, V. Fleischer, H. Zimmermann, A. Droby, J. C. Klein, and R. Deichmann (2016). “Quantitative T1 and proton density mapping with direct calculation of radiofrequency coil transmit and receive profiles from two-point variable flip angle data”. *NMR Biomed.* 29.3, pp. 349–360.
- Bernstein, M. A., K. F. King, and X. J. Zhou (2004). *Handbook of MRI pulse sequences*. Academic Press.
- Büchel, C, T Raedler, M Sommer, M Sach, C Weiller, and M. A. Koch (2004). “White matter asymmetry in the human brain: a diffusion tensor MRI study”. *Cereb. Cortex* 14.9, pp. 945–951.
- Callaghan, M. F., S. Mohammadi, and N. Weiskopf (2016). “Synthetic quantitative MRI through relaxation modelling”. *NMR Biomed.* 29.12, pp. 1729–1738.
- Callaghan, M. F., S. J. Malik, and N. Weiskopf (2015). “Rapid calculation of correction parameters to compensate for imperfect RF spoiling in quantitative R1 mapping”. In: *Proceedings of ISMRM 2015*.

- Callaghan, M. F., P. Freund, B. Draganski, E. Anderson, M. Cappelletti, R. Chowdhury, J. Diedrichsen, T. H. B. Fitzgerald, P. Smittenaar, G. Helms, A. Lutti, and N. Weiskopf (2014). "Widespread age-related differences in the human brain microstructure revealed by quantitative magnetic resonance imaging." *Neurobiol. Aging* 35.8, pp. 1862–1872.
- Callaghan, M. F., G. Helms, A. Lutti, S. Mohammadi, and N. Weiskopf (2015a). "A general linear relaxometry model of R1 using imaging data". *Magn. Reson. Med.* 73.3, pp. 1309–1314.
- Callaghan, M. F., O. Josephs, M. Herbst, M. Zaitsev, N. Todd, and N. Weiskopf (2015b). "An evaluation of prospective motion correction (PMC) for high resolution quantitative MRI". *Front. Neurosci.* 9, p. 97.
- Callaghan, M. F., F. Dick, P. Grabher, T. Keller, P. Freund, and N. Weiskopf (2016). "Optimisation of Post-processing Correction of Transmit Field Inhomogeneity in R1 Maps by Relaxometry Modelling". In: *Proceedings of ISMRM 2016*.
- Carey, D., S. Krishnan, M. F. Callaghan, M. I. Sereno, and F. Dick (2017a). "Functional and Quantitative MRI Mapping of Somatomotor Representations of Human Supralaryngeal Vocal Tract MRI Mapping of Somatomotor Representations of Human Supralaryngeal Vocal Tract". *Cereb. Cortex*. URL: <http://dx.doi.org/10.1093/cercor/bhw393>.
- Carey, D., F. Caprini, M. Allen, A. Lutti, N. Weiskopf, G. Rees, M. F. Callaghan, and F. Dick (2017b). "Quantitative MRI provides markers of intra-, inter-regional, and age-related differences in young adult cortical microstructure". *NeuroImage*. URL: <https://dx.doi.org/10.1016/j.neuroimage.2017.11.066>.
- Castella, R., L. Arn, E. Dupuis, M. F. Callaghan, B. Draganski, and A. Lutti (2018). "Controlling motion artefact levels in MR images by suspending data acquisition during periods of head motion". *Magn. Reson. Med.* URL: <https://dx.doi.org/10.1002/mrm.27214>.
- Chenevert, T. L., D. I. Malyarenko, D. Newitt, X. Li, M. Jayatilake, A. Tudorica, A. Fedorov, R. Kikinis, T. T. Liu, M. Muzi, M. J. Oborski, C. M. Laymon, X. Li, Y. Thomas, K.-C. Jayashree, J. M. Mountz, P. E. Kinahan, D. L. Rubin, F. Fennessy, W. Huang, N. Hylton, and B. D. Ross (2014). "Errors in Quantitative Image Analysis due to Platform-Dependent Image Scaling". *Transl. Oncol.* 7.1, pp. 65–71.
- Chung, S., D. Kim, E. Breton, and L. Axel (2010). "Rapid B1+ mapping using a preconditioning RF pulse with TurboFLASH readout". *Magn. Reson. Med.* 64.2, pp. 439–446.
- Dale, A. M. and M. I. Sereno (1993). "Improved Localizadon of Cortical Activity by Combining EEG and MEG with MRI Cortical Surface Reconstruction: A Linear Approach". *J. Cogn. Neurosci.* 5.2, pp. 162–176.
- Deoni, S. C. L., T. M. Peters, and B. K. Rutt (2005). "High-resolution T1 and T2 mapping of the brain in a clinically acceptable time with DESPOT1 and DESPOT2". *Magn. Reson. Med.* 53.1, pp. 237–241.
- Deoni, S. C. (2007). "High-resolution T1 mapping of the brain at 3T with driven equilibrium single pulse observation of T1 with high-speed incorporation of RF field inhomogeneities (DESPOT1-HIFI)". *J. Magn. Reson. Imaging* 26.4, pp. 1106–1111.
- Deoni, S. C., S. C. Williams, P. Jezzard, J. Suckling, D. G. Murphy, and D. K. Jones (2008). "Standardized structural magnetic resonance imaging in multicentre studies using quantitative T1 and T2 imaging at 1.5 T". *NeuroImage* 40.2, pp. 662–671.
- Dick, F., A. T. Tierney, A. Lutti, O. Josephs, M. I. Sereno, and N. Weiskopf (2012). "In vivo functional and myeloarchitectonic mapping of human primary auditory areas." eng. *J. Neurosci.* 32.46, pp. 16095–16105.
- Dick, F. K., M. I. Lehet, M. F. Callaghan, T. A. Keller, M. I. Sereno, and L. L. Holt (2017). "Extensive Tonal Mapping across Auditory Cortex Is Recapitulated by Spectrally Directed Attention and Systematically Related to Cortical Myeloarchitecture". *J. Neurosci.* 37.50, pp. 12187–12201.
- Does, M. D. (2018). "Inferring brain tissue composition and microstructure via MR relaxometry". *NeuroImage*. URL: <https://dx.doi.org/10.1016/j.neuroimage.2017.12.087>.

- Donahue, K. M., D. Burstein, W. J. Manning, and M. L. Gray (1994). "Studies of Gd-DTPA relaxivity and proton exchange rates in tissue". *Magn. Reson. Med.* 32.1, pp. 66–76.
- Draganski, B., J. Ashburner, C. Hutton, F. Kherif, R. Frackowiak, G. Helms, and N. Weiskopf (2011). "Regional specificity of MRI contrast parameter changes in normal ageing revealed by voxel-based quantification (VBQ)". *NeuroImage* 55.4, pp. 1423–1434.
- Edwards, L. J., E. Kirilina, S. Mohammadi, and N. Weiskopf (2018). "Microstructural imaging of human neocortex in vivo". *NeuroImage*. URL: <https://dx.doi.org/10.1016/j.neuroimage.2018.02.055>.
- Ellerbrock, I. and S. Mohammadi (2018). "Four in vivo g-ratio-weighted imaging methods: Comparability and repeatability at the group level". *Hum. Brain Mapp.* URL: <http://dx.doi.org/10.1002/hbm.23858>.
- Ernst, R. R. and W. A. Anderson (1966). "Application of Fourier Transform Spectroscopy to Magnetic Resonance". *Rev. Sci. Instrum.* 37, pp. 93–102.
- Fatouros, P. P. and A. Marmarou (1999). "Use of magnetic resonance imaging for in vivo measurements of water content in human brain: method and normal values". *J. Neurosurg.* 90.1, pp. 109–115.
- Fatouros, P. P., A. Marmarou, K. A. Kraft, S. Inao, and F. P. Schwarz (1991). "In vivo brain water determination by T1 measurements: effect of total water content, hydration fraction, and field strength". *Magn. Reson. Med.* 17.2, pp. 402–413.
- Fischl, B. and A. M. Dale (2000). "Measuring the thickness of the human cerebral cortex from magnetic resonance images". *Proc. Natl. Acad. Sci. U.S.A.* 97.20, pp. 11050–11055.
- Fischl, B., M. I. Sereno, R. B. Tootell, A. M. Dale, et al. (1999). "High-resolution intersubject averaging and a coordinate system for the cortical surface". *Hum. Brain Mapp.* 8.4, pp. 272–284.
- Focke, N. K., G. Helms, S. Kaspar, C. Diederich, V. Tóth, P. Dechent, A. Mohr, and W. Paulus (2011). "Multi-site voxel-based morphometry—not quite there yet". *NeuroImage* 56.3, pp. 1164–1170.
- Freund, P., N. Weiskopf, J. Ashburner, K. Wolf, R. Sutter, D. R. Altmann, K. Friston, A. Thompson, and A. Curt (2013). "MRI investigation of the sensorimotor cortex and the corticospinal tract after acute spinal cord injury: a prospective longitudinal study". *Lancet Neurol.* 12.9, pp. 873–881.
- Fullerton, G. D., J. L. Potter, and N. C. Dornbluth (1982). "NMR relaxation of protons in tissues and other macromolecular water solutions". *Magn. Reson. Imaging* 1.4, pp. 209–226.
- Gelman, N., J. R. Ewing, J. M. Gorell, E. M. Spickler, and E. G. Solomon (2001). "Interregional variation of longitudinal relaxation rates in human brain at 3.0 T: relation to estimated iron and water contents". *Magn. Reson. Med.* 45.1, pp. 71–79.
- Gorgolewski, K. J., T. Auer, V. D. Calhoun, R. C. Craddock, S. Das, E. P. Duff, G. Flandin, S. S. Ghosh, T. Glatard, Y. O. Halchenko, D. A. Handwerker, M. Hanke, D. Keator, X. Li, Z. Michael, C. Maumet, B. N. Nichols, T. E. Nichols, J. Pellman, J.-B. Poline, A. Rokem, G. Schaefer, V. Sochat, W. Triplett, J. A. Turner, G. Varoquaux, and R. A. Poldrack (2016). "The brain imaging data structure, a format for organizing and describing outputs of neuroimaging experiments". *Sci. Data* 3.160044.
- Griswold, M. A., P. M. Jakob, R. M. Heidemann, M. Nittka, V. Jellus, J. Wang, B. Kiefer, and A. Haase (2002). "Generalized autocalibrating partially parallel acquisitions (GRAPPA)". *Magn. Reson. Med.* 47.6, pp. 1202–1210.
- Helbling, S., S. Teki, M. F. Callaghan, W. Sedley, S. Mohammadi, T. D. Griffiths, N. Weiskopf, and G. R. Barnes (2015). "Structure predicts function: Combining non-invasive electrophysiology with in-vivo histology". *NeuroImage* 108, pp. 377–385.
- Helms, G. (2015). "Correction for residual effects of B1+ inhomogeneity on MT saturation in FLASH-based multi-parameter mapping of the brain". In: *Proceedings of ISMRM 2015*.
- Helms, G., H. Dathe, and P. Dechent (2008). "Quantitative FLASH MRI at 3T Using a Rational Approximation of the Ernst Equation". *Magn. Reson. Med.* 59, pp. 667–672.
- Helms, G. and G. E. Hagberg (2009). "In vivo quantification of the bound pool T_1 in human white matter using the binary spin-bath model of progressive magnetization transfer saturation". *Phys. Med. Biol.* 54.23, N529–N540.

- Helms, G., H. Dathe, K. Kallenberg, and P. Dechent (2008). "High-resolution maps of magnetization transfer with inherent correction for RF inhomogeneity and T1 relaxation obtained from 3D FLASH MRI." *Magn. Reson. Med.* 60.6, pp. 1396–1407.
- Helms, G., B. Draganski, R. Frackowiak, J. Ashburner, and N. Weiskopf (2009). "Improved segmentation of deep brain grey matter structures using magnetization transfer (MT) parameter maps". *NeuroImage* 47.1, pp. 194–198.
- Helms, G., H. Dathe, N. Weiskopf, and P. Dechent (2011). "Identification of signal bias in the variable flip angle method by linear display of the algebraic ernst equation". *Magn. Reson. Med.* 66.3, pp. 669–677.
- Heule, R., C. Ganter, and O. Bieri (2015). "Variable flip angle T_1 mapping in the human brain with reduced t_2 sensitivity using fast radiofrequency-spoiled gradient echo imaging". *Magn. Reson. Med.* 75.4, pp. 1413–1422.
- Kamman, R. L., K. G. Go, W. Brouwer, and H. J. Berendsen (1988). "Nuclear magnetic resonance relaxation in experimental brain edema: Effects of water concentration, protein concentration, and temperature". *Magn. Reson. Med.* 6.3, pp. 265–274.
- Kaneoke, Y., M. Furuse, S. Inao, K. Saso, K. Yoshida, Y. Motegi, M. Mizuno, and A. Izawa (1987). "Spin-lattice relaxation times of bound water—its determination and implications for tissue discrimination". *Magn. Reson. Imaging* 5.6, pp. 415–420.
- Lambert, C., A. Lutti, G. Helms, R. Frackowiak, and J. Ashburner (2013). "Multiparametric brainstem segmentation using a modified multivariate mixture of Gaussians". *NeuroImage: Clinical* 2, pp. 684–694.
- Lee, J. E., M. K. Chung, M. Lazar, M. B. DuBray, J. Kim, E. D. Bigler, J. E. Lainhart, and A. L. Alexander (2009). "A study of diffusion tensor imaging by tissue-specific, smoothing-compensated voxel-based analysis". *NeuroImage* 44.3, pp. 870–883.
- Lee, J., Y. Nam, J. Y. Choi, E. Y. Kim, S.-H. Oh, and D.-H. Kim (2016). "Mechanisms of T2* anisotropy and gradient echo myelin water imaging". *NMR Biomed.* 30.4, e3513.
- Lee, Y., M. F. Callaghan, and Z. Nagy (2017). "Analysis of the Precision of Variable Flip Angle T1 Mapping with Emphasis on the Noise Propagated from RF Transmit Field Maps". *Front. Neurosci.* 11, p. 106.
- Lee, Y., M. F. Callaghan, J. Acosta-Cabronero, A. Lutti, and Z. Nagy (2018). "Establishing Intra- and Inter-vendor Reproducibility of T1 Relaxation Time Measurements with 3T MRI". *Magn. Reson. Med.* URL: <https://doi.org/10.1002/mrm.27421>.
- Liberman, G., Y. Louzoun, and D. Ben Bashat (2013). "T1 Mapping using variable flip angle SPGR data with flip angle correction". *J. Magn. Reson. Imaging* 40.1, pp. 171–180.
- Lorio, S., A. Lutti, F. Kherif, A. Ruef, J. Dukart, R. Chowdhury, R. Frackowiak, J. Ashburner, G. Helms, N. Weiskopf, and B. Draganski (2014). "Disentangling in vivo the effects of iron content and atrophy on the ageing human brain". *NeuroImage* 103, pp. 280–289.
- Lorio, S., S. Fresard, S. Adaszewski, F. Kherif, R. Chowdhury, R. Frackowiak, J. Ashburner, G. Helms, N. Weiskopf, A. Lutti, and B. Draganski (2016a). "New tissue priors for improved automated classification of subcortical brain structures on MRI". *NeuroImage* 130, pp. 157–166.
- Lorio, S., F. Kherif, A. Ruef, L. Melie-Garcia, R. Frackowiak, J. Ashburner, G. Helms, A. Lutti, and B. Draganski (2016b). "Neurobiological origin of spurious brain morphological changes: A quantitative MRI study". *Hum. Brain Mapp.* 37.5, pp. 1801–1815.
- Lutti, A., C. Hutton, and N. Weiskopf (2009). "Optimization of 3D EPI technique for radio frequency (B1) field mapping at 3T". In: *Proceedings of ISMRM 2009*, p. 2797.
- Lutti, A. and N. Weiskopf (2013). "Optimizing the Accuracy of T1 Mapping Accounting for RF Non-Linearities and Spoiling Characteristics in FLASH Imaging". In: *Proceedings of ISMRM 2013*.
- Lutti, A., C. Hutton, J. Finsterbusch, G. Helms, and N. Weiskopf (2010). "Optimization and validation of methods for mapping of the radiofrequency transmit field at 3T". *Magn. Reson. Med.* 64.1, pp. 229–238.

- Lutti, A., J. Stadler, O. Josephs, C. Windischberger, O. Speck, J. Bernarding, C. Hutton, and N. Weiskopf (2012). "Robust and Fast Whole Brain Mapping of the RF Transmit Field B₁ at 7T". *PLoS ONE* 7.3, pp. 1–7.
- Lutti, A., F. Dick, M. I. Sereno, and N. Weiskopf (2014). "Using high-resolution quantitative mapping of R₁ as an index of cortical myelination". *NeuroImage* 93, pp. 176–188.
- Marques, J. P., D. Khabipova, and R. Gruetter (2017). "Studying cyto and myeloarchitecture of the human cortex at ultra-high field with quantitative imaging: R₁, R₂^{*} and magnetic susceptibility". *Neuroimage* 147, pp. 152–163.
- Mazziotta, J., A. Toga, A. Evans, P. Fox, J. Lancaster, K. Zilles, R. Woods, T. Paus, G. Simpson, B. Pike, and et al. (2001a). "A Four-Dimensional Probabilistic Atlas of the Human Brain". *J. Am. Med. Assoc.* 8.5, pp. 401–430.
- (2001b). "A probabilistic atlas and reference system for the human brain: International Consortium for Brain Mapping (ICBM)". *Philos. Trans. R. Soc. B Biol. Sci.* 356.1412, pp. 1293–1322.
- Mazziotta, J. C., A. W. Toga, A. Evans, P. Fox, and J. Lancaster (1995). "A Probabilistic Atlas of the Human Brain: Theory and Rationale for Its Development: The International Consortium for Brain Mapping (ICBM)". *NeuroImage* 2.2, Part A, pp. 89–101.
- Mezer, A., A. Rokem, S. Berman, T. Hastie, and B. A. Wandell (2016). "Evaluating quantitative proton-density-mapping methods". *Hum. Brain Mapp.* 37.10, pp. 3623–3635.
- Mohammadi, S. and M. F. Callaghan (2018). "Quantitative MRI of the Brain: Principles of Physical Measurement". In: ed. by M. Cercignani, N. G. Dowell, and P. S. Tofts. 2nd. Series in Medical Physics and Biomedical Engineering. CRC Press. Chap. Image Analysis, pp. 303–324.
- Mohammadi, S., S. S. Keller, V. Glauche, H. Kugel, A. Jansen, C. Hutton, A. Flöel, and M. Deppe (2012). "The influence of spatial registration on detection of cerebral asymmetries using voxel-based statistics of fractional anisotropy images and TBSS". *PLoS ONE* 7.6, e36851.
- Mohammadi, S., K. Tabelow, L. Ruthotto, T. Feiweier, J. Polzehl, and N. Weiskopf (2014). "High-resolution diffusion kurtosis imaging at 3T enabled by advanced post-processing". *Front. Neurosci.* 8, p. 427.
- Mohammadi, S., D. Carey, F. Dick, J. Diedrichsen, M. I. Sereno, M. Reisert, M. F. Callaghan, and N. Weiskopf (2015). "Whole-Brain In-vivo Measurements of the Axonal G-Ratio in a Group of 37 Healthy Volunteers". *Front. Neurosci.* 9, p. 441.
- Oh, S.-H., Y.-B. Kim, Z.-H. Cho, and J. Lee (2013). "Origin of B₀ orientation dependent R₂^{*} (=1/T₂^{*}) in white matter". *NeuroImage* 73, pp. 71–79.
- Papp, D., M. F. Callaghan, H. Meyer, C. Buckley, and N. Weiskopf (2016). "Correction of inter-scan motion artifacts in quantitative R₁ mapping by accounting for receive coil sensitivity effects". *Magn. Reson. Med.* 76.5, pp. 1478–1485.
- Pohmann, R. and K. Scheffler (2013). "A theoretical and experimental comparison of different techniques for B₁ mapping at very high fields". *NMR Biomed.* 26.3, pp. 265–275.
- Polzehl, J. and K. Tabelow (2016). "Low SNR in diffusion MRI models". *J. Amer. Statist. Assoc.* 111.516, pp. 1480–1490.
- Preibisch, C. and R. Deichmann (2009). "Influence of RF spoiling on the stability and accuracy of T₁ mapping based on spoiled FLASH with varying flip angles." *Magn. Reson. Med.* 61.1, pp. 125–135.
- Pruessmann, K. P., M. Weiger, M. B. Scheidegger, and P. Boesiger (1999). "SENSE: Sensitivity encoding for fast MRI". *Magn. Reson. Med.* 42.5, pp. 952–962.
- Reisert, M., I. Mader, R. Umarova, S. Maier, L. Tebartz van Elst, and V. G. Kiselev (2013). "Fiber density estimation from single q-shell diffusion imaging by tensor divergence". *NeuroImage* 77, pp. 166–176.
- Reuter, M., M. D. Tisdall, A. Qureshi, R. L. Buckner, A. J. van der Kouwe, and B. Fischl (2015). "Head motion during MRI acquisition reduces gray matter volume and thickness estimates". *NeuroImage* 107, pp. 107–115.

- Ridgway, G. R., S. M. D. Henley, J. D. Rohrer, R. I. Scahill, J. D. Warren, and N. C. Fox (2008). "Ten simple rules for reporting voxel-based morphometry studies". *NeuroImage* 40.4, pp. 1429–1435.
- Rosen, A. F., D. R. Roalf, K. Ruparel, J. Blake, K. Seelaus, L. P. Villa, R. Ciric, P. A. Cook, C. Davatzikos, M. A. Elliott, A. G. de La Garza, E. D. Gennatas, M. Quarmley, J. E. Schmitt, R. T. Shinohara, M. D. Tisdall, R. C. Craddock, R. E. Gur, R. C. Gur, and T. D. Satterthwaite (2018). "Quantitative assessment of structural image quality". *NeuroImage* 169, pp. 407–418.
- Ruthotto, L., S. Mohammadi, C. Heck, J. Modersitzki, and N. Weiskopf (2013). "Hyperelastic Susceptibility Artifact Correction of DTI in SPM". In: *Bildverarbeitung für die Medizin 2013*. Ed. by H.-P. Meinzer, T. M. Deserno, H. Handels, and T. Tolxdorff. Berlin, Heidelberg: Springer Berlin Heidelberg, pp. 344–349.
- Schabel, M. C. and G. R. Morrell (2008). "Uncertainty in T1 mapping using the variable flip angle method with two flip angles". *Phys. Med. Biol.* 54.1, N1–N8.
- Seif, M., T. Leutritz, R. S. Samson, A. Curt, C. A. G. Wheeler-Kingshott, P. Freund, and N. Weiskopf (2018). "A multi-center study on fast full-brain quantitative multi-parameter mapping of R1, MT, and R2*: Scan-rescan repeatability and inter-site reproducibility". In: *Proceedings of ISMRM 2018*, p. 1199.
- Sereno, M. I., A. Lutti, N. Weiskopf, and F. Dick (2013). "Mapping the human cortical surface by combining quantitative T1 with retinotopy." eng. *Cereb. Cortex* 23.9, pp. 2261–2268.
- Shuter, B., S. C. Wang, J. Roche, G. Briggs, and J. M. Pope (1998). "Relaxivity of Gd-EOB-DTPA in the normal and biliary obstructed guinea pig". *J. Magn. Reson. Imaging* 8.4, pp. 853–861.
- Smith, S. M., M. Jenkinson, H. Johansen-Berg, D. Rueckert, T. E. Nichols, C. E. Mackay, K. E. Watkins, O. Ciccarelli, M. Z. Cader, P. M. Matthews, and T. E. J. Behrens (2006). "Tract-based spatial statistics: voxelwise analysis of multi-subject diffusion data". *NeuroImage* 31.4, pp. 1487–1505.
- Soares, J. M., P. Marques, V. Alves, and N. Sousa (2013). "A hitchhiker's guide to diffusion tensor imaging". *Front. Neurosci.* 7, p. 31.
- Sotiropoulos, S. N., S. Jbabdi, J. Xu, J. L. Andersson, S. Moeller, E. J. Auerbach, M. F. Glasser, M. Hernandez, G. Sapiro, M. Jenkinson, D. A. Feinberg, E. Yacoub, C. Lenglet, D. C. Van Essen, K. Ugurbil, T. E. J. Behrens, and WU-Minn HCP Consortium (2013). "Advances in diffusion MRI acquisition and processing in the Human Connectome Project". *NeuroImage* 80, pp. 125–143.
- Steiger, T. K., N. Weiskopf, and N. Bunzeck (2016). "Iron Level and Myelin Content in the Ventral Striatum Predict Memory Performance in the Aging Brain". *J. Neurosci.* 36.12, pp. 3552–3558.
- Stikov, N., L. M. Perry, A. Mezer, E. Rykhlevskaia, B. A. Wandell, J. M. Pauly, and R. F. Dougherty (2011). "Bound pool fractions complement diffusion measures to describe white matter micro and macrostructure". *NeuroImage* 54.2, pp. 1112–1121.
- Stikov, N., J. S. W. Campbell, T. Stroh, M. Lavelée, S. Frey, J. Novek, S. Nuara, M.-K. Ho, B. J. Bedell, R. F. Dougherty, I. R. Leppert, M. Boudreau, S. Narayanan, T. Duval, J. Cohen-Adad, P.-A. Picard, A. Gasecka, D. Côté, and G. B. Pike (2015). "In vivo histology of the myelin g-ratio with magnetic resonance imaging". *NeuroImage* 118, pp. 397–405.
- Stüber, C., M. Morawski, A. Schäfer, C. Labadie, M. Wähnert, C. Leuze, M. Streicher, N. Barapatre, K. Reimann, S. Geyer, D. Spemann, and R. Turner (2014). "Myelin and iron concentration in the human brain: a quantitative study of MRI contrast". *NeuroImage* 93 Pt 1, pp. 95–106.
- Tabelow, K., S. Mohammadi, N. Weiskopf, and J. Polzehl (2015). "POAS4SPM: A Toolbox for SPM to Denoise Diffusion MRI Data". *Neuroinformatics* 13.1, pp. 19–29.
- Tabelow, K., C. D'Alonzo, J. Polzehl, M. F. Callaghan, L. Ruthotto, N. Weiskopf, and S. Mohammadi (2016). "How to achieve very high resolution quantitative MRI at 3T". In: *Proceedings of HBM 2016*.
- Tabelow, K., C. D'Alonzo, L. Ruthotto, M. F. Callaghan, N. Weiskopf, J. Polzehl, and S. Mohammadi (2017). "Removing the estimation bias due to the noise floor in multi-parameter maps". In: *Proceedings of ISMRM 2017*.
- Tofts, P., ed. (2004). *Quantitative MRI of the Brain: Measuring Changes Caused by Disease*. Wiley.

- Tofts, P. S. (2003). "PD: Proton Density of Tissue Water". In: *Quantitative MRI of the Brain: Measuring Changes Caused by Disease*. Ed. by P. S. Tofts. Chichester, UK: Wiley & Sons, pp. 85–110.
- Tofts, P. S., S. C. Steens, and M. A. van Buchem (2004). "MT: Magentization Transfer". In: *Quantitative MRI of the Brain: Measuring Changes Caused by Disease*. Ed. by P. S. Tofts. Wiley.
- Trampel, R., P.-L. Bazin, K. Pine, and N. Weiskopf (2017). "In-vivo magnetic resonance imaging (MRI) of laminae in the human cortex". *NeuroImage*. URL: <https://doi.org/10.1016/j.neuroimage.2017.09.037>.
- Volz, S., U. Nöth, A. Rotarska-Jagiela, and R. Deichmann (2010). "A fast B1-mapping method for the correction and normalization of magnetization transfer ratio maps at 3T". *NeuroImage* 49.4, pp. 3015–3026.
- Volz, S., U. Nöth, A. Jurcoane, U. Ziemann, E. Hattingen, and R. Deichmann (2012). "Quantitative proton density mapping: correcting the receiver sensitivity bias via pseudo proton densities". *NeuroImage* 63.1, pp. 540–552.
- Wang, H. Z., S. J. Riederer, and J. N. Lee (1987). "Optimizing the precision in T1 relaxation estimation using limited flip angles". *Magn. Reson. Med.* 5.5, pp. 399–416.
- Weiskopf, N. and G. Helms (2008). "Multi-parameter mapping of the human brain at 1mm resolution in less than 20 minutes". In: *Proceedings of ISMRM 2008*. 2241.
- Weiskopf, N., A. Lutti, G. Helms, M. Novak, J. Ashburner, and C. Hutton (2011). "Unified segmentation based correction of R1 brain maps for RF transmit field inhomogeneities (UNICORT)". *NeuroImage* 54.3, pp. 2116–2124.
- Weiskopf, N., J. Suckling, G. Williams, M. M. Correia, B. Inkster, R. Tait, C. Ooi, E. T. Bullmore, and A. Lutti (2013). "Quantitative multi-parameter mapping of R1, PD(*), MT, and R2(*) at 3T: a multi-center validation." *Front. Neurosci.* 7, p. 95.
- Weiskopf, N., M. F. Callaghan, O. Josephs, A. Lutti, and S. Mohammadi (2014). "Estimating the apparent transverse relaxation time (R2(*)) from images with different contrasts (ESTATICS) reduces motion artifacts." *Front. Neurosci.* 8, p. 278.
- Weiskopf, N., S. Mohammadi, A. Lutti, and M. F. Callaghan (2015). "Advances in MRI-based computational neuroanatomy". *Curr. Opin. Neurol.* 28.4, pp. 313–322.
- Wharton, S. and R. Bowtell (2012). "Fiber orientation-dependent white matter contrast in gradient echo MRI". *Proc. Natl. Acad. Sci. U.S.A.* 109.45, pp. 18559–18564.
- Whitaker, K. J., P. E. Vértes, R. Romero-Garcia, F. Váša, M. Moutoussis, G. Prabhu, N. Weiskopf, M. F. Callaghan, K. Wagstyl, T. Rittman, and et al. (2016). "Adolescence is associated with genomically patterned consolidation of the hubs of the human brain connectome". *Proc. Natl. Acad. Sci. U.S.A.* 113.32, pp. 9105–9110.
- Yarnykh, V. L. (2007). "Actual flip-angle imaging in the pulsed steady state: A method for rapid three-dimensional mapping of the transmitted radiofrequency field". *Magn. Reson. Med.* 57.1, pp. 192–200.
- Yarnykh, V. L. (2010). "Optimal radiofrequency and gradient spoiling for improved accuracy of T1 and B1 measurements using fast steady-state techniques". *Magn. Reson. Med.* 63.6, pp. 1610–1626.
- Yendiki, A., P. Panneck, P. Srinivasan, A. Stevens, L. Zöllei, J. Augustinack, R. Wang, D. Salat, S. Ehrlich, T. Behrens, S. Jbabdi, R. Gollub, and B. Fischl (2011). "Automated probabilistic reconstruction of white-matter pathways in health and disease using an atlas of the underlying anatomy". *Front. Neuroinform.* 5, p. 23.
- Ziegler, G., P. Grabher, A. Thompson, D. Altmann, M. Hupp, J. Ashburner, K. Friston, N. Weiskopf, A. Curt, and P. Freund (2018). "Progressive neurodegeneration following spinal cord injury". *Neurology* 90.14, e1257–e1266.